

Elemental cryo-imaging reveals SOS1-dependent vacuolar sodium accumulation

<https://doi.org/10.1038/s41586-024-08403-y>

Received: 3 December 2023

Accepted: 5 November 2024

Published online: 15 January 2025

Open access

 Check for updates

Priya Ramakrishna^{1,2}✉, Francisco M. Gámez-Arjona^{3,4,9}, Etienne Bellani^{1,2,9}, Cristina Martín-Olmos^{1,5}, Stéphane Escrig¹, Damien De Bellis^{2,6}, Anna De Luca⁴, José M. Pardo⁴, Francisco J. Quintero⁴, Christel Genoud^{6,7}, Clara Sánchez-Rodríguez^{3,8}, Niko Geldner²✉ & Anders Meibom^{1,5}✉

Increasing soil salinity causes significant crop losses globally; therefore, understanding plant responses to salt (sodium) stress is of high importance. Plants avoid sodium toxicity through subcellular compartmentation by intricate processes involving a high level of elemental interdependence. Current technologies to visualize sodium, in particular, together with other elements, are either indirect or lack in resolution. Here we used the newly developed cryo nanoscale secondary ion mass spectrometry ion microprobe¹, which allows high-resolution elemental imaging of cryo-preserved samples and reveals the subcellular distributions of key macronutrients and micronutrients in root meristem cells of *Arabidopsis* and rice. We found an unexpected, concentration-dependent change in sodium distribution, switching from sodium accumulation in the cell walls at low external sodium concentrations to vacuolar accumulation at stressful concentrations. We conclude that, in root meristems, a key function of the NHX family sodium/proton antiporter SALT OVERLY SENSITIVE1 (also known as Na⁺/H⁺ exchanger 7; SOS1/NHX7) is to sequester sodium into vacuoles, rather than extrusion of sodium into the extracellular space. This is corroborated by the use of new genomic, complementing fluorescently tagged SOS1 variants. We show that, in addition to the plasma membrane, SOS1 strongly accumulates at late endosome/prevacuoles as well as vacuoles, supporting a role of SOS1 in vacuolar sodium sequestration.

Cells accumulate a restricted set of elements within a specific range of concentrations to sustain their metabolic activities. Element-selective transport across the plasma membrane and into specific subcellular organelles is thus fundamental to life^{2,3}. This has driven evolution of an elaborate network of channels and transporters that dynamically regulate strong concentration differences with the surroundings, as well as intracellularly between subcellular compartments⁴. In terrestrial plants, even relatively small deviations from elemental homeostasis can have profound consequences for organismal function, including failure to grow and reproduce⁵. Most agricultural plants are very sensitive to the presence of sodium (Na) in the soil (referred to as salt stress), which today results in an estimated annual crop loss of 20–40% (ref. 6). Conditions leading to salt stress are exacerbated by climate change and are thus becoming an urgent problem for a growing world population.

Despite the importance of sodium detoxification for survival of plants in saline soils, efforts to obtain a mechanistic understanding of elemental homeostasis and cellular adaptation to salt stress have been hampered by the inability to directly observe element distributions

within cells at sufficient resolution. Genetically encoded fluorescent sensors and element-specific dyes provide indirect measures of one element at a time and are often restricted to a specific subcellular compartment. They can also be limited in sensitivity or dynamic range. Mass spectrometry or X-ray-based analytical techniques, such as laser ablation inductively coupled plasma mass spectrometry (LA-ICP-MS), X-ray fluorescence microscopy or energy dispersive X-ray spectroscopy either lack the spatial resolution or the sensitivity to detect intracellular elemental distributions. Furthermore, these generally require sample preparation involving dehydration, which unavoidably results in loss and/or substantial redistribution of solutes^{7–11}. Building on previous work^{12–14}, we have recently developed a cryo nanoscale secondary ion mass spectrometry (CryoNanoSIMS) ion microprobe that integrates with a fully cryogenic workflow, including block face cryo-scanning electron microscope (cryoSEM) imaging of vitrified samples. This new approach permits us to obtain elemental and isotope maps of vitrified biological tissues in their most pristine state with unparalleled sensitivity, mass and image resolution, and without any loss or displacement of soluble compounds¹.

¹Laboratory for Biological Geochemistry, School of Architecture, Civil and Environmental Engineering, Ecole Polytechnique Fédérale de Lausanne (EPFL), Lausanne, Switzerland. ²Department of Plant Molecular Biology, Biophore, UNIL-Sorge, University of Lausanne, Lausanne, Switzerland. ³Department of Biology, ETH Zürich, Zürich, Switzerland. ⁴Institute of Plant Biochemistry and Photosynthesis, Consejo Superior de Investigaciones Científicas and Universidad de Sevilla, Seville, Spain. ⁵Center for Advanced Surface Analysis, Institute of Earth Sciences, University of Lausanne, Lausanne, Switzerland. ⁶Electron Microscopy Facility, University of Lausanne, Lausanne, Switzerland. ⁷Life Sciences, Ecole Polytechnique Fédérale de Lausanne, Lausanne, Switzerland. ⁸Centro de Biotecnología y Genómica de Plantas, Universidad Politécnica de Madrid (UPM) – Instituto Nacional de Investigación y Tecnología Agraria y Alimentaria (INIA/CSIC), Pozuelo de Alarcón, Spain. ⁹These authors contributed equally: Francisco M. Gámez-Arjona, Etienne Bellani. ✉e-mail: priya.ramakrishna@epfl.ch; niko.geldner@unil.ch; anders.meibom@epfl.ch

Here we performed correlated cryoSEM and CryoNanoSIMS imaging to shed light on the cellular mechanisms underlying the salt-stress response in plants (Fig. 1a–c). We use *Arabidopsis thaliana* (*Arabidopsis*) root meristems as a model, but also demonstrate the applicability of our technique to *Oryza sativa* (rice), a global crop, in which we confirm our major findings. Root meristems carry the vital stem cell populations from which the entire root body originates. They explore new soil areas and are arguably the first to encounter, and locally deal with, excessive sodium concentrations. The ability of root meristems to extrude or compartmentalize sodium is therefore a major determinant of a plant's ability to maintain growth at a given soil salinity.

Figure 1 schematically illustrates the general workflow (Fig. 1a) and examples of the resulting correlated cryoSEM image and CryoNanoSIMS maps (Fig. 1b,c). To facilitate direct comparison between different roots, clearly defined meristematic root zones were systematically mapped with CryoNanoSIMS; namely, the region in which the cells transition from division to elongation (Extended Data Fig. 1c). Using this workflow, we demonstrate that we can obtain parallel, high-resolution elemental maps for up to seven key elements, measured by their major stable isotopes: ^{23}Na , ^{24}Mg , ^{32}S , ^{39}K , ^{40}Ca , ^{55}Mn and ^{56}Fe (Fig. 1c). Validating our method, the observed subcellular elemental distributions in *Arabidopsis* root tips grown on a standard liquid half-strength Murashige–Skoog (MS) medium are highly consistent with specific predictions (Fig. 1c). Calcium, for example, is known to have low cytosolic concentrations and to accumulate in the cell wall¹⁵, which is consistent with the CryoNanoSIMS calcium map (Fig. 1c). Moreover, calcium maps exhibited hot-spots in the wall and cell corners, which are likely to be correlated with the presence of pectins (negatively charged, galacturonic acid-based polymers) that cross-link with calcium¹⁵. On the other hand, magnesium (known to interact with phospholipid membranes, proteins and phospho-nucleotides; in particular, ATP)¹⁶ was observed in the cytosol and vacuoles (Fig. 1c). Sodium and potassium, the elements of direct interest to this study, displayed strongly contrasting distributions, with sodium concentrated primarily in the extracellular space and potassium preferentially accumulating in the cytosol, where it acts as the major monovalent cation (Fig. 1c).

In contrast to animals, most plant species do not require sodium for any vital cellular process and grow well in its absence. We used a mini-hydroponics system to grow *Arabidopsis* plants, to obtain full control over elemental concentrations in the medium (Extended Data Fig. 1a). As expected, our CryoNanoSIMS detected only few counts of sodium when seedlings were grown on a sodium-free (Na-free) medium (control condition) (Fig. 2a and Extended Data Fig. 2a). By contrast, both low levels of sodium (half-strength MS medium, approx. 0.1 mM Na⁺; Extended Data Fig. 2c) and slightly elevated sodium levels (2.5 mM NaCl; Fig. 2b, Extended Data Fig. 2d) resulted in a strong increase of sodium in the cell wall (Extended Data Fig. 2g), and a relatively low, but clearly detectable, presence of sodium in the cytosol (Extended Data Fig. 2e,f). This suggests either active sodium export, or limited uptake of sodium as the mechanism that maintains low cytosolic sodium levels under mild salt stress. The sodium/proton antiporter SOS1/NHX7 of the NHX family of antiporters is a major determinant of salt tolerance in *Arabidopsis*. It is expressed strongly in the root meristem that we investigated and is thought to act at the plasma membrane for extrusion of sodium into the cell wall^{17–19}. Interestingly, already at these low sodium concentrations (2.5 mM NaCl), a mutant of SOS1 (*sos1-1; sos1* from now on) showed increased cytosolic Na:K ratios and a decrease in Na:Ca ratios in the cell wall, which would be consistent with a function of SOS1 in sodium export at these concentrations (Extended Data Fig. 2d–g).

However, when we increased the salt stress to moderate levels (25 mM NaCl for 4 h) we observed a radical change in the subcellular distribution of sodium (Fig. 2c). Meristematic cells then displayed strong accumulation of sodium in their vacuoles, with relatively less sodium in the cell walls (Fig. 2c,d and Extended Data Fig. 3a–c). By contrast, *sos1*

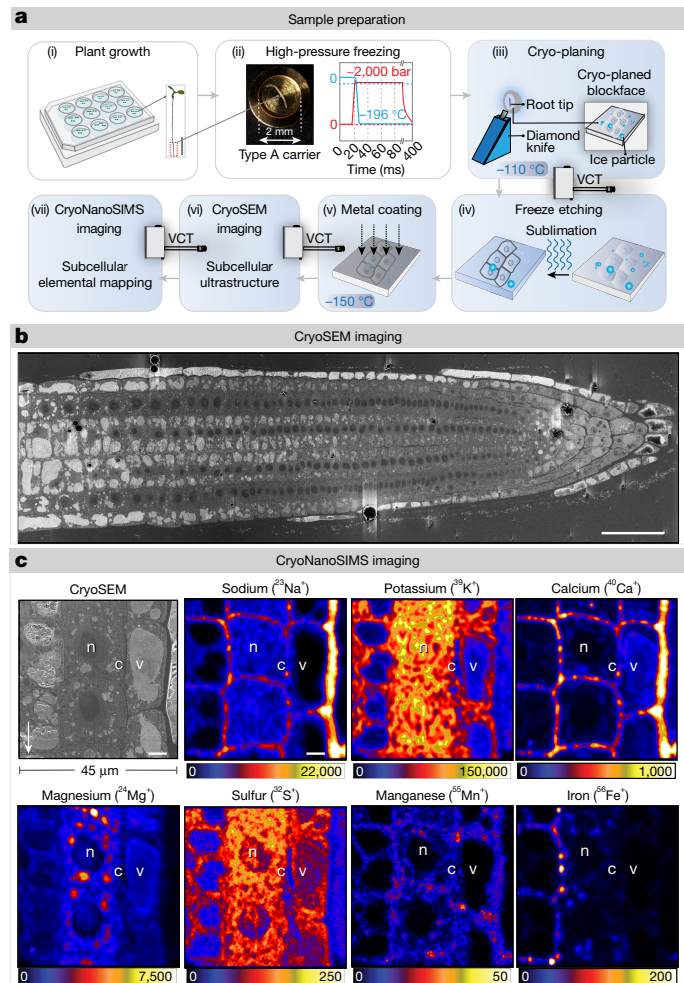


Fig. 1 | Cryogenic workflow and correlative block face cryoSEM–CryoNanoSIMS imaging of *Arabidopsis* roots. **a**, (i) Schematic of *Arabidopsis* seedlings grown in a 12-well hydroponics culture dish. Inset, image of 5-day-old seedlings from which root tips were sampled for high-pressure freezing. (ii) Vitrification by high-pressure freezing showing a root segment cut approximately 3 mm from the tip placed in a type A carrier filled with cryoprotectant. The graph illustrates the freezing process, with rapid build-up of pressure to approximately 2,000 bar accompanied by cooling with liquid N₂ to -196°C , vitrifying the sample. From this point on, the sample was maintained and handled under cryo-conditions. (iii) Vitrified root samples were cryo-planed to create a flat block face suitable for imaging. The sample was then transferred to an evaporator with a VCT shuttle. (iv) The block face was sublimated (freeze etched) to remove surface ice contamination and bring out ultrastructural detail of the root. (v) The sample surface was then coated and shuttled with the VCT into the cryoSEM. (vi) Tissue ultrastructure was imaged with cryoSEM. (vii) The sample was recoated and shuttled into the CryoNanoSIMS for elemental imaging. For more details, see Methods. **b**, CryoSEM imaged longitudinal view of a cryo-planed *Arabidopsis* root tip grown on liquid half-strength MS medium exhibiting the ultrastructural details of root meristem cells in their pristine, vitrified state. **c**, Example of a high-resolution cryoSEM image directly correlated with CryoNanoSIMS elemental maps of a cryo-planed root tip of WT *Arabidopsis* grown on liquid half-strength MS medium and treated as described in **a**, revealing the tissue organization and intracellular distributions of Na, K, Ca, Mg, S, Mn and Fe. Vacuole (v), cytoplasm (c) and nucleus (n) are labelled. Colour scales are linear and maximum count rates (counts per second) are indicated by the colour bars. Scale bars, 1 cm (a), 45 μm (b), 5 μm (c).

mutants showed the opposite sodium distribution, with low sodium in the vacuoles and much higher sodium in the cytosol (Fig. 2c,d), producing a reversal of vacuole:cytosol ratios compared with wild type (WT)

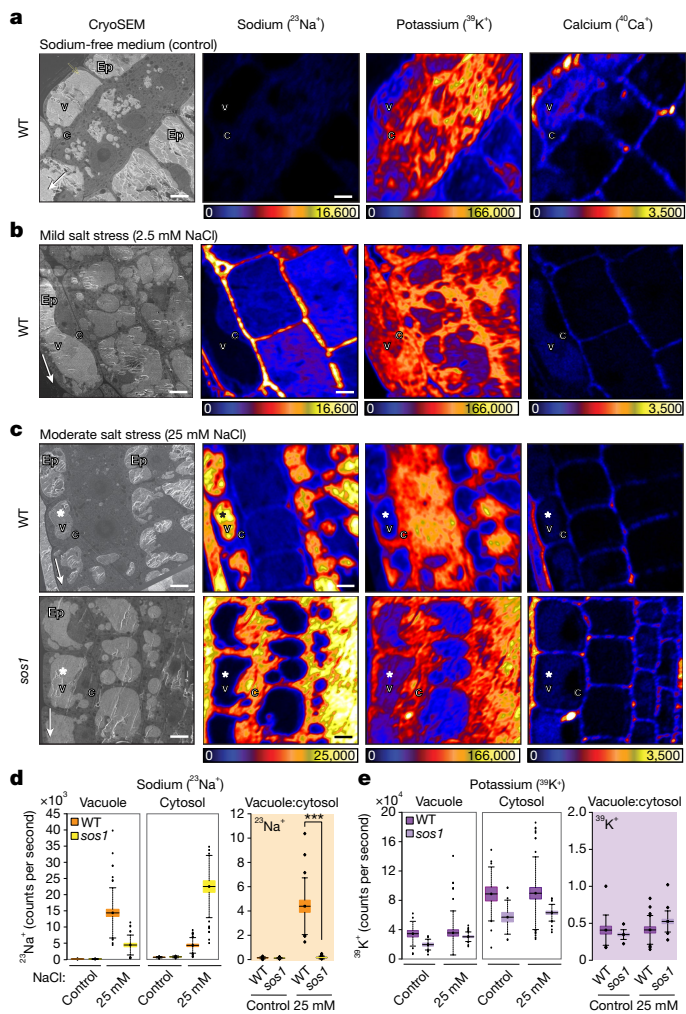


Fig. 2 | Correlated cryoSEM and CryoNanoSIMS mapping of Na⁺, K⁺ and Ca²⁺ in root meristems of *Arabidopsis* WT and *sos1* mutant under mild and moderate salt stress. a, Representative images of WT seedlings grown on a Na-free medium (control), characterized by low, but clearly measurable background Na levels before salt-stress experiments; compare with Extended Data Fig. 2a,b for *sos1*. Epidermis (Ep), vacuole (v) and cytoplasm (c) are labelled. b, Root meristem of WT seedlings treated with 2.5 mM NaCl for 2 h (mild salt stress); compare with Extended Data Fig. 2d for *sos1*. c, Root meristem of WT and *sos1* seedlings incubated with 25 mM NaCl for 4 h (moderate salt stress). Note that WT cells accumulated Na into vacuoles (*), whereas *sos1* mutants accumulated Na in the cytosol. d, Average count rates for sodium ($^{23}\text{Na}^+$) in the vacuole and cytosol of the meristem cells in WT and *sos1* (left) after growth in Na-free medium (control) and after treatment with 25 mM NaCl for 4 h. Also shown are vacuole:cytosol count-rate ratios of $^{23}\text{Na}^+$ within individual meristem cells in WT and *sos1* (right, orange). e, Corresponding average count rates for potassium ($^{39}\text{K}^+$) in the vacuole and cytosol of the meristem cells in WT and *sos1* (left). Also shown are vacuole:cytosol count-rate ratios of $^{39}\text{K}^+$ within individual meristem cells in WT and *sos1* after growth (right, lilac). The intracellular distribution of potassium did not change significantly with the treatment. Box plots show the mean values (horizontal lines), 25% (boxes) and 75% (thin vertical bars) quartiles; outliers are indicated with solid circles. The samples were hydroponically grown on a Na-free medium and subject to respective treatments. Colour scales are linear and maximum ion count rates (counts per second) are indicated by the colour bars. Thin white arrows in cryoSEM images point towards the root tip. Scale bars, 5 μm .

(Fig. 2d and Extended Data Fig. 3b). This revealed that the *sos1* mutant is impaired in sodium translocation into vacuoles. However, at this level of salt stress and despite the substantial build-up of sodium in *sos1* cytosol, the intracellular distribution of potassium, that is, the

potassium vacuole:cytosol ratio, was not yet perturbed (Fig. 2c–e and Extended Data Fig. 3b).

At higher levels of salt stress (100 mM NaCl for 4 h), WT root meristem cells remained capable of concentrating sodium in their vacuoles and thus maintained a low cytosolic sodium level (Fig. 3a). The *sos1* mutant, by contrast, suffered an even stronger build-up of sodium in its cytosol, associated with some degree of vacuolar accumulation (Fig. 3a–c and Extended Data Fig. 3d,e). Importantly, a concomitant drop in cytosolic potassium was observed in *sos1*, but not in WT (Fig. 3a,c), leading to a dramatic change of the cytosolic Na:K ratio in *sos1*, compared with WT (Fig. 3c). The observed decrease in cytosolic potassium ions and the appearance of sodium ions in the vacuoles in *sos1* under high salt stress (Fig. 3a), is consistent with the often-proposed notion of sodium toxicity being due to a displacement of potassium as a counterion for cytosolic proteins^{20,21}. Indeed, WT plants were able to recover from this acute salt stress and even maintain slow growth on 100 mM NaCl on agar plates, whereas longer exposure of *sos1* mutants to this salt concentration caused a complete cessation of growth from which *sos1* did not recover, in contrast to WT (Extended Data Fig. 5d–f).

Based on our data in *Arabidopsis* root meristematic cells, the detoxification strategy of sodium sequestration in the cell wall, either through export or inhibition of uptake, appears relevant only at low sodium concentrations. Already at moderate salt stress, a new mechanism based on vacuolar or prevacuolar sequestration appears to dominate over export to reduce sodium concentration in the cytosol (Figs. 2 and 3). As root meristems were previously not considered to use sodium vacuolar sequestration as a protective mechanism, we wanted to see whether this mechanism is more broadly conserved. For this, we used root meristems of rice, as a major crop and a representative of the divergent monocot branch of flowering plants. Intriguingly, we observed the same, strong vacuolar accumulation upon salt stress, with maintenance of high potassium-to-sodium ratios in the cytosol (Fig. 3d and Extended Data Fig. 4b–e), demonstrating the conservation of this mechanism among angiosperms. In contrast to *Arabidopsis*, where *SOS1* is expressed in both root meristem and differentiated vascular tissue, the rice *SOS1* ortholog is not expressed in root meristems, but is exclusive to the differentiated root vasculature (Extended Data Fig. 4a)²². We therefore predicted that the observed vacuolar accumulation in rice root meristems should not be dependent on *OsSOS1*. Indeed, we found the same pattern of vacuolar accumulation of sodium in the rice *sos1* mutant as that observed in WT rice (Extended Data Fig. 4b–e). Thus, other transporters, such as of the endosomal or vacuolar NHX members, probably mediate vacuolar translocation in rice meristematic cells. The observed differences between *OsSOS1* and *AtSOS1* are most likely not to be due to any differences in the cellular or biochemical activity of the proteins, because *OsSOS1* under the control of a constitutive promoter fully rescues the *Arabidopsis sos1* phenotype²³.

SOS1 has long been thought to be localized exclusively to the plasma membrane¹⁸ where it mediates sodium export into the cell wall. However, our data show that, under elevated sodium concentrations, the SOS1 protein has a dominant role in sodium accumulation into vacuoles (Figs. 2 and 3). New structural data shows SOS1 as a 13 transmembrane-spanning domain protein with an extracellular N-terminus and cytosolic C-terminus²⁴ (Extended Data Fig. 5a). Current knowledge of SOS1 localization is entirely based on overexpression of fluorescent cDNA fusion constructs in a WT background¹⁹. We therefore generated two independent genomic fusion constructs of SOS1. One contained a 1,929 bp promoter region linked to the coding sequence, including the first 13 introns, a nopaline synthase (NOS)-terminator and green fluorescent protein tag (*SOS1-GFP*). The other had a larger 2,250 bp promoter fragment with the full number of introns and an endogenous SOS1 3'UTR-terminator fragment (*SOS1-mCitrine*) (Extended Data Fig. 5b,c). In *Arabidopsis* seedlings, both fusion constructs largely complemented the salt sensitivity phenotype of *sos1* (Extended Data Fig. 5d–h) and gave very similar subcellular localization

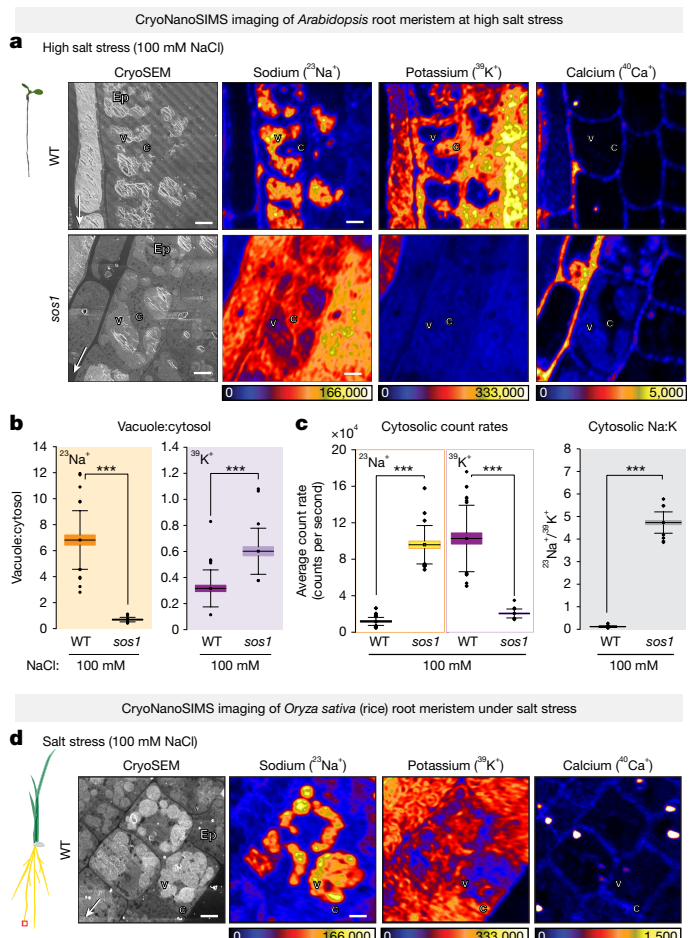


Fig. 3 | Correlated cryoSEM and CryoNanoSIMS mapping of Na⁺, K⁺ and Ca²⁺ in root meristems of *Arabidopsis* WT and *sos1* mutant and rice WT under high salt stress. **a**, Representative images of epidermal cells from WT and *sos1* treated with 100 mM NaCl for 4 h. Note the maintenance of low Na levels in WT cytosol, in contrast with the strong accumulation of Na in *sos1* cytosol. Note also a significant decrease in the cytosolic K in *sos1* cells compared with the WT. Epidermis (Ep), vacuole (v) and cytoplasm (c) are labelled. **b**, Vacuole:cytosol count-rate ratios of ²³Na⁺ (left) and ³⁹K⁺ (right) from root epidermal meristem cells in WT and *sos1* on 100 mM NaCl for 4 h. **c**, Average count rates for ²³Na⁺ and ³⁹K⁺ in the cytosol of the meristem cells in WT and *sos1* (left) and the corresponding average cytosolic Na:K ratios (right). Note the maintenance of low sodium levels in WT cytosol, in contrast with the strong cytosolic sodium accumulation in *sos1*, and a significant decrease in the cytosolic potassium in *sos1* compared with the WT. **d**, Representative images of rice root meristem epidermal cells under salt stress. WT seedlings were treated with 100 mM NaCl for 4 h. Note that WT cells accumulated Na into vacuoles similarly to WT *Arabidopsis*. The experiment was repeated twice with similar results. See Extended Data Fig. 4 for comparative analysis with rice *sos1* mutant. Box plots show the mean values (horizontal lines), 25% (boxes) and 75% (thin vertical bars) quartiles; outliers are indicated with solid circles. Samples were grown in hydroponics on Na-free medium and subject to respective treatments. Colour scales are linear and maximum ion count rates (counts per second) are indicated by the colour bars. Thin white arrows in SEM images point towards the root tip. Scale bars, 5 μm.

with rather weak signals (Fig. 4a and Extended Data Fig. 6a). The former construct variant showed a consistently higher, more easily observable signal than the latter and was therefore used for most experiments presented here (Fig. 4a). Surprisingly, our complementing fusion constructs showed strong accumulation in undefined endomembrane compartments, of both reticulate and vesicle-like nature, and some degree of tonoplast accumulation, in addition to its reported plasma

membrane localization (Fig. 4a). When quantified, the SOS1 fluorescence signal measured in endomembrane compartments largely surpassed that at the plasma membrane (Fig. 4b). These endomembrane compartments did not significantly colocalize with the endocytic tracer FM4-64 (1 h uptake) (Extended Data Figs. 6a and 8a) nor with the early endosome/trans-Golgi network marker VHA-a1 (Fig. 4c, Extended Data Fig. 6b and Supplementary Video 1). The presence of SOS1 on both prevacuolar/late endosomal and vacuolar membranes was confirmed by colocalization and comigration with late endosomal Rab markers (Fig. 4d,e, Extended Data Fig. 6b and Supplementary Video 2) and colocalization with the vacuolar SNARE protein mCherry-VAMP711 (VESICLE-ASSOCIATED MEMBRANE PROTEIN 711) (Fig. 4f and Extended Data Fig. 6c)²⁵. We observed no change in SOS1 localization upon salt stress (Fig. 4c–f right panel and Extended Data Fig. 6b,e), except for its enhancement at the plasma membrane, as previously reported²⁶ and a different appearance of the tonoplast, due to a known change of vacuolar structures. SOS1-positive vesicle-like structures showed clear colocalization and comigration with late endosomal/prevacuolar compartment markers, as was evident in time-lapse analyses (Extended Data Fig. 6d and Supplementary Video 2). Consistently, on application of the PI3 kinase inhibitor Wortmannin, known to affect RabF-positive compartments, SOS1-GFP and RABF2A were seen to colocalize in swollen Wortmannin-induced prevacuolar structures (Extended Data Fig. 7). By contrast, Brefeldin A (BFA), which inhibits early and recycling endosomes, only caused weak accumulation of SOS1-GFP in 'BFA bodies', which further supported its late endosomal localization (Extended Data Fig. 8b–d). We could further demonstrate that the observed vacuolar localization of SOS1 is not due to the presence of fluorescent protein tag, nor to a specificity of root meristem cells. We detected endogenous SOS1 on vacuolar membrane fractions prepared from leaves, using a purified peptide antibody (Extended Data Fig. 8e). This was corroborated by clear SOS1-GFP signals on vacuolar preparations of *Arabidopsis* mesophyll cells (Extended Data Fig. 8f).

The additional late endosomal and vacuolar localization observed here is fully consistent with an activity of SOS1 in vacuolar sodium sequestration, as suggested by the CryoNanoSIMS data (Figs. 2 and 3). Indeed, the large surface-to-volume ratios of the prevacuolar endosomal compartments might be advantageous for efficient clearing of sodium from the cytosol and sequestration into luminal spaces that eventually fuse with the vacuole and deliver their contents. Such a mechanism for sodium sequestration was previously proposed, based on the unexpected importance of endosomal (as opposed to vacuolar) proton-pump activities for sodium tolerance^{27,28}.

Previous observations of sodium in planta often confounded many cell types within organs or complex tissues^{29,30}. The application of our new high-resolution elemental imaging technology to plants has allowed us to describe the unexpected complexity of the sodium detoxification within single root meristem cells, involving retention in the cell wall and vacuolar sequestration, depending on salt-stress intensity. Our CryoNanoSIMS observations, in combination with the unexpected subcellular localization of the central sodium/proton antiporter SOS1 to late endosomal and vacuolar membranes, demonstrate that SOS1 is critically involved in vacuolar sodium sequestration in addition to its role of sodium efflux at the cell surface. In the case of xylem loading, for example, clear evidence supports a plasma membrane-based activity of SOS1, counteracting the activity of HKT1 that promotes sodium retention in roots, as well as in other organs³¹. This cycle might allow rapid switching of root retention of sodium towards transport to aerial tissues upon increases in sodium concentrations²⁰. The absence of a differentiated vasculature in root meristems might render a sodium extrusion strategy ineffective and explain a critical role of vacuolar accumulation as a detoxification strategy for these crucially important meristem cells. It is important to note that our work with the CryoNanoSIMS probe allows us to obtain *in situ* data, not of transport, but of subcellular ion distribution, for which we compare mutant and WT. Therefore,

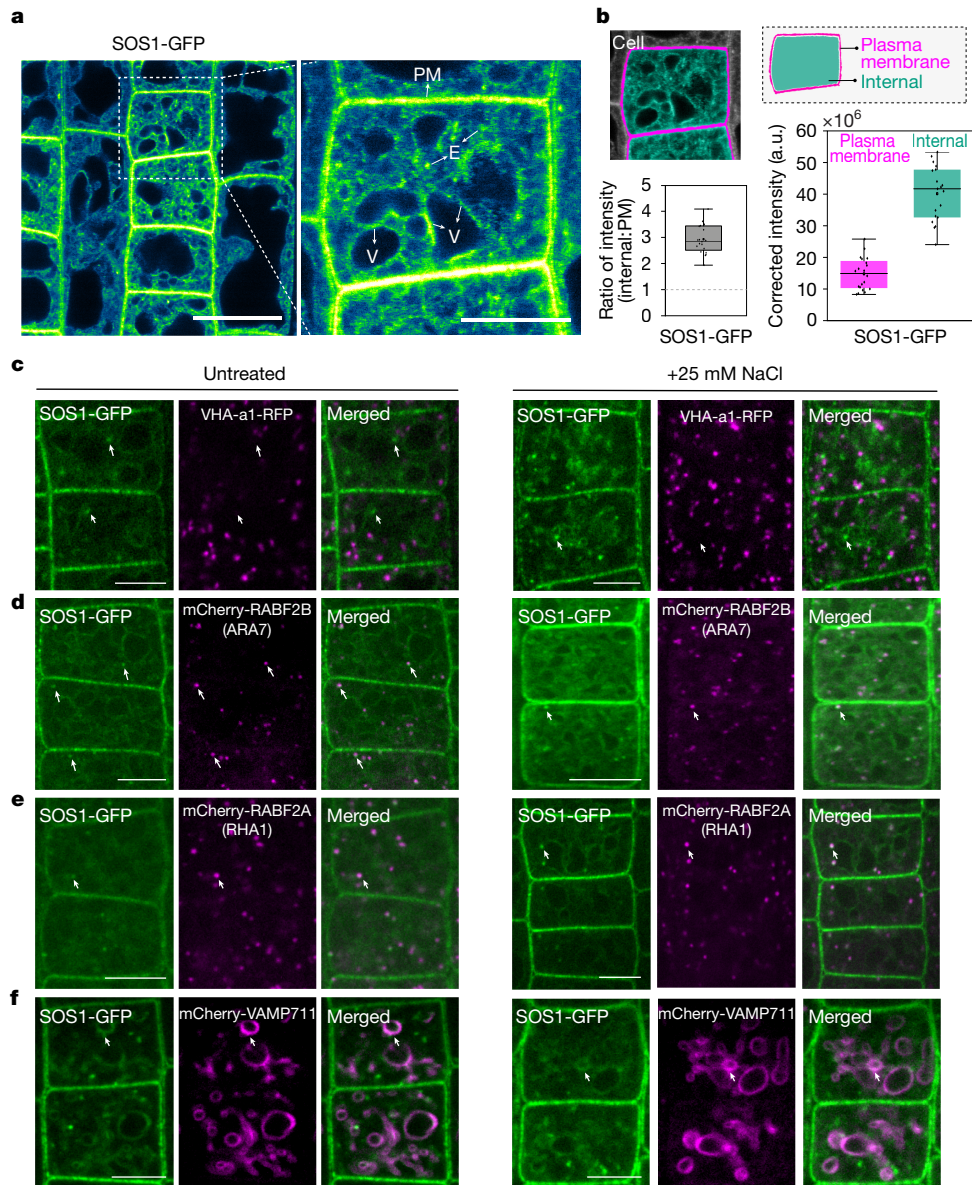


Fig. 4 | Subcellular localization of sodium/proton antiporter SOS1. **a**, Localization of SOS1-GFP in *Arabidopsis* root epidermal cells in *sos1* complemented lines. Close-up view of an epidermal cell (area marked with dotted box). Note the strong signal from endomembrane compartments in addition to the plasma membrane (PM). The arrows highlight endomembrane compartments (E) and vacuoles (V). **b**, Quantification of the SOS1-GFP signal measured in the plasma membrane and inside the cell (internal), as shown in the schematic, and the corresponding ratio of the SOS1-GFP signal (internal:PM). Corrected intensity is given in arbitrary units (a.u.). **c**, SOS1 protein did not colocalize with the *trans*-Golgi network marker VHA-a1 in the root epidermal cells. Absence of colocalization can be observed in Supplementary Video 1. **d**, SOS1-GFP showed partial association with mCherry-RABF2B (ARA7). Arrows highlight selected punctate points that show the association. **e**, SOS1-GFP

partial association with mCherry-RABF2A (RHA1). For tracking of vesicle comigration, compare with Extended Data Fig. 5b and Supplementary Video 2. **f**, SOS1-GFP (green) displayed significant colocalization with the tonoplast marker mCherry-VAMP711 (magenta). For all the markers, the localization upon 25 mM NaCl treatment for 1 day is shown by corresponding images on the right. The seedlings for **a** and **b** were grown in growth condition 1 and for **c–f** they were grown in growth condition 2 (Methods). Quantification of SOS1-GFP signal, $n = 20$ cells from four different roots examined independently. Box plots show the median values (horizontal lines), 25% (boxes) and 75% (thin vertical bars) quartiles, and the mean is represented by the square symbol within the box. For quantification of vesicle association, refer to Extended Data Fig. 6b and Supplementary Videos 1 and 2. Scale bars, 20 μm (**a** (overview)), 10 μm (**a** (inset), **c–f**).

rather than replacing transport measurements, our method adds an important new dimension to our understanding of the intricacies of salt detoxification in plants. Actual, traditional transport measurements are evidently irreplaceable but are very difficult to execute for specific organelles in specific cell types.

SOS1/NHX7 is highly selective for sodium transport whereas all other intracellular NHX variants tested so far discriminate poorly between sodium and potassium as transport substrates³². Nevertheless, our results in rice show that, although vacuolar sodium accumulation

in root meristems is conserved, transporters other than SOS1 must mediate this accumulation. Based on our results, it will be important to reassess the role of the SOS1 homologs of the NHX family with Cryo-NanoSIMS, as several NHX family members have been localized to vacuolar and endosomal compartments and are thought to mediate vacuolar sequestration independently of SOS1 (refs. 30,33). Consistent with our findings, it was reported that absence of all vacuolar NHX family members (NHX1–4) of *Arabidopsis* did not abrogate vacuolar accumulation of NaCl in *Arabidopsis*, an activity that might be mediated

by vacuolar-localized SOS1 (ref. 34). Interestingly, a recent report on the highly salt-tolerant plant species *Salicornia bigelovii* found the presence of a putative ortholog of SOS1 in vacuolar membrane fractions of leaf tissues³⁵. It was suggested that this presents a case of neo-functionalization of SOS1 in this highly salt-adapted plant, for vacuolar sequestration instead of extrusion into the cell wall. Instead, our data suggests that vacuolar sequestration is actually a conserved function of SOS1, as we find endosomal/vacuolar localization of SOS1 not only in root meristematic cells, but also in leaf tissue of *Arabidopsis*, which is a glycophyte with a salt tolerance much more similar to all major crop species.

In a broader perspective, we have demonstrated that CryoNanoSIMS enables direct, multi-elemental imaging at subcellular resolution, not only in *Arabidopsis*, but also in rice, as a major crop and monocot model species. This promises to lead to breakthroughs in our understanding of elemental homeostasis in plants, by addressing a broad range of fundamental questions concerning acquisition and distribution of other agronomically important macronutrients such as potassium, calcium and magnesium; particularly when combined with already available and characterized transport mutants. Moreover, CryoNanoSIMS has the potential to provide insights into the *in vivo* roles of many as yet unidentified, or insufficiently characterized transporters. Finally, we have demonstrated that even micronutrients or trace elements, such as iron or manganese, can be imaged with this technology (Fig. 1c). Another currently unexplored area of great potential will be the use of isotopes for elemental flux measurements, to allow their uptake and distribution to be traced.

Online content

Any methods, additional references, Nature Portfolio reporting summaries, source data, extended data, supplementary information, acknowledgements, peer review information; details of author contributions and competing interests; and statements of data and code availability are available at <https://doi.org/10.1038/s41586-024-08403-y>.

- Meibom, A. et al. Correlated cryo-SEM and CryoNanoSIMS imaging of biological tissue. *BMC Biol.* **21**, 126 (2023).
- Dubyak, G. R. Ion homeostasis, channels, and transporters: an update on cellular mechanisms. *Adv. Physiol. Educ.* **28**, 143–154 (2004).
- Nelson, N. Metal ion transporters and homeostasis. *EMBO J.* **18**, 4361–4371 (1999).
- White, P. J. in *Marschner's Mineral Nutrition of Higher Plants (Third edition)* (ed. Marschner, P.) 7–47 (Academic, 2012).
- Römhild, V. in *Marschner's Mineral Nutrition of Higher Plants (Third edition)* (ed. Marschner, P.) 299–312 (Academic, 2012).
- Vargas, R. et al. (eds) *Handbook for Saline Soil Management* (Food and Agriculture Organization of the United Nations, Lomonosov Moscow State Univ., 2018).
- Kim, S. A. et al. Localization of iron in *Arabidopsis* seed requires the vacuolar membrane transporter VIT1. *Science* **314**, 1295–1298 (2006).
- Persson, D. P. et al. Multi-element bioimaging of *Arabidopsis thaliana* roots. *Plant Physiol.* **172**, 835–847 (2016).
- Moore, K. L. et al. Combined NanoSIMS and synchrotron X-ray fluorescence reveal distinct cellular and subcellular distribution patterns of trace elements in rice tissues. *New Phytol.* **201**, 104–115 (2014).
- Rowan, A., McCully, M. E. & Canny, M. J. The origin of the exudate from cut maize roots. *Plant Physiol. Biochem.* **38**, 957–967 (2000).
- Chia, J.-C. et al. Loss of OPT3 function decreases phloem copper levels and impairs crosstalk between copper and iron homeostasis and shoot-to-root signaling in *Arabidopsis thaliana*. *Plant Cell* **35**, 2157–2185 (2023).

- Metzner, R., Schneider, H. U., Breuer, U. & Schroeder, W. H. Imaging nutrient distributions in plant tissue using time-of-flight secondary ion mass spectrometry and scanning electron microscopy. *Plant Physiol.* **147**, 1774–1787 (2008).
- Chandra, S., Bernius, M. T. & Morrison, G. H. Intracellular localization of diffusible elements in frozen-hydrated biological specimens with ion microscopy. *Anal. Chem.* **58**, 493–496 (1986).
- Dérue, C. et al. Dynamic-SIMS imaging and quantification of inorganic ions in frozen-hydrated plant samples. *Microsc. Res. Tech.* **69**, 53–63 (2006).
- Palin, R. & Geitmann, A. The role of pectin in plant morphogenesis. *BioSystems* **109**, 397–402 (2012).
- Roman, A. M. P. in *Magnesium in the Central Nervous System* (eds Vink, R. & Nechifor, M.) Ch. 2 (Univ. Adelaide Press, 2011).
- Wu, S. J., Ding, L. & Zhu, J. K. SOS1, a genetic locus essential for salt tolerance and potassium acquisition. *Plant Cell* **8**, 617–627 (1996).
- Shi, H., Ishitani, M., Kim, C. & Zhu, J.-K. The *Arabidopsis thaliana* salt tolerance gene SOS1 encodes a putative Na⁺/H⁺ antiporter. *Proc. Natl Acad. Sci. USA* **97**, 6896–6901 (2000).
- Shi, H., Quintero, F. J., Pardo, J. M. & Zhu, J.-K. The putative plasma membrane Na⁺/H⁺ antiporter SOS1 controls long-distance Na⁺ transport in plants. *Plant Cell* **14**, 465–477 (2002).
- Maathuis, F. K. nutrition and Na⁺ toxicity: the basis of cellular K⁺/Na⁺ ratios. *Ann. Bot.* **84**, 123–133 (1999).
- Benito, B., Haro, R., Amtmann, A., Cuin, T. A. & Dreyer, I. The twins K⁺ and Na⁺ in plants. *J. Plant Physiol.* **171**, 723–731 (2014).
- El Mahi, H. et al. A critical role of sodium flux via the plasma membrane Na⁺/H⁺ exchanger SOS1 in the salt tolerance of rice. *Plant Physiol.* **180**, 1046–1065 (2019).
- Martinez-Atienza, J. et al. Conservation of the salt overly sensitive pathway in rice. *Plant Physiol.* **143**, 1001–1012 (2007).
- Wang, Y. et al. Architecture and autoinhibitory mechanism of the plasma membrane Na⁺/H⁺ antiporter SOS1 in *Arabidopsis*. *Nat. Commun.* **14**, 4487 (2023).
- Geldner, N. et al. Rapid, combinatorial analysis of membrane compartments in intact plants with a multicolor marker set. *Plant J.* **59**, 169–178 (2009).
- Gámez-Arjona, F. et al. Inverse regulation of SOS1 and HKT1 protein localization and stability by SOS3/CBL4 in *Arabidopsis thaliana*. *Proc. Natl Acad. Sci. USA* **121**, e2320657121 (2024).
- Krebs, M. et al. *Arabidopsis* V-ATPase activity at the tonoplast is required for efficient nutrient storage but not for sodium accumulation. *Proc. Natl Acad. Sci. USA* **107**, 3251–3256 (2010).
- Hamaji, K. et al. Dynamic aspects of ion accumulation by vesicle traffic under salt stress in *Arabidopsis*. *Plant Cell Physiol.* **50**, 2023–2033 (2009).
- Kronzucker, H. J. & Britto, D. T. Sodium transport in plants: a critical review. *New Phytol.* **189**, 54–81 (2011).
- Apse, M. P., Aharon, G. S., Snedden, W. A. & Blumwald, E. Salt tolerance conferred by overexpression of a vacuolar Na⁺/H⁺ antiport in *Arabidopsis*. *Science* **285**, 1256–1258 (1999).
- Uchiyama, T. et al. The HKT1 Na⁺ transporter protects plant fertility by decreasing Na⁺ content in stamen filaments. *Sci. Adv.* **9**, eadg5495 (2023).
- Raddatz, N., Morales de los Ríos, L., Lindahl, M., Quintero, F. J. & Pardo, J. M. Coordinated transport of nitrate, potassium, and sodium. *Front. Plant Sci.* **11**, 247 (2020).
- Bassil, E. et al. The *Arabidopsis* intracellular Na⁺/H⁺ antiporters NHX5 and NHX6 are endosome associated and necessary for plant growth and development. *Plant Cell* **23**, 224–239 (2011).
- Bassil, E., Zhang, S., Gong, H., Tajima, H. & Blumwald, E. Cation specificity of vacuolar NHX-type cation/H⁺ antiporters. *Plant Physiol.* **179**, 616–629 (2019).
- Salazar, O. R. et al. SOS1 tonoplast neo-localization and the RGG protein SALTY are important in the extreme salinity tolerance of *Salicornia bigelovii*. *Nat. Commun.* **15**, 4279 (2024).

Publisher's note Springer Nature remains neutral with regard to jurisdictional claims in published maps and institutional affiliations.



Open Access This article is licensed under a Creative Commons Attribution-NonCommercial-NoDerivatives 4.0 International License, which permits any non-commercial use, sharing, distribution and reproduction in any medium or format, as long as you give appropriate credit to the original author(s) and the source, provide a link to the Creative Commons licence, and indicate if you modified the licensed material. You do not have permission under this licence to share adapted material derived from this article or parts of it. The images or other third party material in this article are included in the article's Creative Commons licence, unless indicated otherwise in a credit line to the material. If material is not included in the article's Creative Commons licence and your intended use is not permitted by statutory regulation or exceeds the permitted use, you will need to obtain permission directly from the copyright holder. To view a copy of this licence, visit <http://creativecommons.org/licenses/by-nc-nd/4.0/>.

© The Author(s) 2025

Methods

Plant materials

For the experiments, *Arabidopsis thaliana* ecotype Columbia-0 (Col-0) referred to as WT and *salt overly sensitive 1 (sos1)* mutant in the Col-0 *gl-1* background were used; the *sos1-1* allele was previously identified in an ethyl methane sulfonate screen¹⁷. The following published constructs were introduced either by transformation or crossing into *sos1:SOS1-GFP* (ref. 26); *VHA-A1-RFP* (AT2G28520: VACUOLAR PROTON ATPASE A1); *mCherry-RABF2A* (AT5G45130: RHA1 or ARABIDOPSIS RAB HOMOLOG F2A); *mCherry-RABF2B* (AT4G19640: ARA7 or ARABIDOPSIS RAB GTPASE HOMOLOG F2B); *mCherry-VAMP711* (AT4G32150: VESICLE-ASSOCIATED MEMBRANE PROTEIN 711) (refs. 25,36). Rice (*Oryza sativa*) cv. Nipponbare (WT) and the mutant *Ossos1* are lines previously described²².

Hydroponics plant growth

Seedlings grown under standard conditions on standard half-strength Murashige–Skoog (MS) media agar plates were exposed to low and variable levels of Na, which resulted in a high Na-background in the CryoNanoSIMS images. To ensure a controlled starting point for subsequent salt-stress experiments, a growth medium free of Na was required. This was achieved with a hydroponics system and using a medium formulation free of sodium (referred throughout the manuscript as Na-free medium) to allow fully controlled salt-stress assays for growth experiments.

Composition of liquid MS and Na-free medium for hydroponics. The Na-free medium was composed of MS basal salt macronutrient solution (formulation number M0654; Sigma-Aldrich) as the macroelement source. Each microelement solution was prepared separately and all solutions were prepared with MilliQ water. Essential micronutrients, free from Na-containing compounds, were used at the following concentrations: 50 µM boric acid (H_3BO_3), 0.05 µM copper sulfate pentahydrate ($CuSO_4 \cdot 5H_2O$), 0.01 µM molybdic acid ammonium salt heptahydrate ($(NH_4)_6 Mo_7O_{24} \cdot 4H_2O$), 2.5 µM potassium iodide (KI), 0.05 µM cobalt(II) chloride hexahydrate ($CoCl_2 \cdot 6H_2O$), 50 µM Fe(III)-EDTA ($C_{10}H_{12}FeN_2O_8$) (Chemie Brunschwig AG, CH), 50 µM manganese(II) sulfate monohydrate ($MnSO_4 \cdot 2H_2O$) and 50 µM zinc sulfate heptahydrate ($ZnSO_4 \cdot 7H_2O$). 2.5 mM MES (2-morpholinoethanesulfonic acid) buffer was added, the pH was adjusted to 5.7 with KOH and the solution was sterilized. For comparison with a liquid half-strength MS medium, the seedlings were grown on a sterile liquid half-strength MS solution, pH adjusted to 5.7 with KOH.

Arabidopsis growth. Sterilized *Arabidopsis* seeds were sown on a wetted perforated disc placed in a sterile 12-well culture plate and stratified in the dark for 2 days. The pore size of the disc was approximately 120 µm, which prevented the seeds from falling through, but was sufficient for the roots to grow through. Post stratification, the wells were carefully topped with 4 ml of Na-free medium which enabled the discs with the seeds to float. The set-up was transferred to growth chambers at 21 °C with constant light and grown for 5 days. For NaCl treatments, stock solutions prepared in MilliQ water were used and the seedlings were directly treated with 2.5 mM, 25 mM and 100 mM NaCl for the indicated times in the hydroponics system under sterile condition and subsequently sampled for analysis with the cryogenic workflow described below (Fig. 1a). Root growth in the hydroponics system was compared with standard half-strength MS growth medium and growth on agar plates (Extended Data Fig. 1a). The concentrations of Na for growth stress were tested on agar plates and treatment conditions selected for hydroponics treatment (Extended Data Fig. 1d).

Rice growth. Sterilized rice seeds were germinated on wet filter paper for 3 days in the dark and then transferred to a hydroponics system on perforated sterile filter paper with the cotyledon in contact with the same Na-free medium described above. Growth was continued in a

hydroponics settings in the growth chamber set to 28 °C with constant light and grown for 5 days. Salt treatments were given by adding NaCl directly to the hydroponic set-up and then sampled for high-pressure freezing (see below) at the set time point.

CryoSEM–CryoNanoSIMS workflow

A general description of the CryoNanoSIMS workflow can be found in ref. 1. Here we describe a specific workflow optimized for plants that focusing on *Arabidopsis* root meristems, as illustrated in Fig. 1 and Extended Data Fig. 1.

Sample preparation and high-pressure freezing. This process is schematically summarized in Fig. 1a. For high-pressure freezing, the seedlings were gently transferred to a small petri dish with the media. The roots (radius approximately 120 µm) were cut approximately 3 mm from the tip and immediately placed in a 3-mm-diameter gold coated Type A Cu-carrier with a cavity of 0.1 mm (Article 1322, Wohlwend GmbH, Sennwald, Switzerland) filled with the cryoprotectant Dextran 40 (25% w/v in 50 mM MES, pH 5.7) and then covered with the flat side of an aluminium specimen carrier type B (Article 1313, Wohlwend GmbH, Sennwald, Switzerland) and directly high-pressure frozen using an EM ICE (Leica) device. From this point on in the workflow, the samples were maintained and handled under strictly controlled cryo-conditions.

Cryo-planing of vitrified sample block face. The Cu-carriers with the root samples were loaded into a sample holder inside a Leica instrument EM VCM with a stable cryo-environment (liquid N_2 bath) and transferred to a Leica cryo-chamber EM FC7 on a Leica EM UC7 Ultramicrotome with the chamber and the sample holder maintained at -110 °C. A flat and smooth surface, which is essential for CryoNanoSIMS imaging, was created with a trimming diamond knife Cryo TRIM20 (Diatome, Biel), generating a surface block face containing a section of the root sample. A diamond cryo TRIM20 Diatome knife was used to further smooth the surface of the sample.

From this point on, a Leica EM VCT500 vacuum cryo-transfer (VCT) shuttle, holding the sample at about -150 °C in a vacuum of 8×10^{-4} mbar, was used to transfer the sample between different instruments.

Freeze etching. The samples were transferred to a Leica cryo-eBeam metal coater EM ACE600 under cryogenic conditions, pumped to a vacuum of 9×10^{-7} mbar. Samples were sublimated with a temperature cycle in which they were ramped up from -150 °C to -94 °C over 20 min, held at -94 °C for 90 s and ramped down to -150 °C over 20 min with a ramp rate of 3 °C min⁻¹. These settings were empirically optimized to remove surface ice contamination and gently bring out ultrastructural detail of the root sections, which could be imaged in the cryoSEM.

Metal coating and cryoSEM imaging. Before cryoSEM imaging, the sample surface was coated with an approximately 3 nm layer of PtC using Leica cryo-eBeam metal coater (EM ACE600). The roots were then imaged using a Zeiss Gemini 500 SEM with a Leica cryostage operated at -140 °C with the vacuum at 2.7×10^{-8} mbar. Images were acquired with the Inlens detector and an accelerating voltage of 1.7 kV with a working distance of 3.5 mm and an aperture size of 10 µm. High-resolution images of 4,098 × 3,072 pixels were obtained both for overviews of the root samples and at higher magnification from areas of interest at the surface of the sample. These cryoSEM images served to select and correlate regions of the root sections with CryoNanoSIMS imaging.

Second metal coating. The samples were returned with the VCT under vacuum from the cryoSEM to the Leica cryo-eBeam metal coater EM ACE600. An additional approximately 17 nm layer of PtC was deposited on the sample surface and maintained at -150 °C. This was necessary to increase the conductivity and dissipate surface charging during

CryoNanoSIMS analysis. The sample was then transferred with the VCT to the CryoNanoSIMS for imaging.

CryoNanoSIMS imaging. Elemental mapping was performed with the new CryoNanoSIMS instrument within the Laboratory for Biological Geochemistry at EPFL¹. Images were systematically acquired on the root meristem with epidermal cells in the region where the cells transition from division to elongation (Extended Data Figs. 1c and 4a). Sample surface areas with ice or particle contamination (visible in cryoSEM images) were avoided. Areas selected for imaging were presputtered for 5 min with a defocused 16 keV O⁻ ion beam to a total dose of about 1.5×10^{16} O⁻ ions per cm², to remove the metal coating. The sample surface was then bombarded with a primary ion beam of about 20 pA O⁻ ions focused to a spot size of about 400 nm. Images of $45 \times 45 \mu\text{m}^2$ with 256×256 pixels were obtained by rastering this primary beam across the sample surface with a pixel dwell time of 5 ms. Secondary ions ²³Na⁺, ²⁴Mg⁺, ³²S⁺, ³⁹K⁺, ⁴⁰Ca⁺, ⁵⁵Mn⁺ and ⁵⁶Fe⁺ were simultaneously collected in electron multipliers at a mass resolution of about 7,000 (Cameca definition), which was enough to resolve all mass interferences. A total of six acquisition cycles were recorded for a total analysis time of about 35 min per image (Extended Data Fig. 1b). Importantly, with these analytical settings, ²³Na⁺ and ³⁹K⁺, the two ions of direct importance for this study, were clearly detectable in all parts of the plant tissue from all experimental conditions (Extended Data Fig. 2), rendering a statistically robust direct comparison of the relative sodium and potassium distributions possible.

NanoSIMS image processing and analysis. Image analysis was performed using the L'IMAGE software v.10-15-2021 (developed by L. Nittler). Layers were drift corrected and accumulated. Regions of interest (ROIs) were drawn on ion images based on cryoSEM images to demarcate cells and the two primary subcellular areas of interest: vacuoles and cytosol (Extended Data Fig. 1e). For the 2.5 mM treatment, ROIs for the cell wall were conservatively selected with the calcium ion map as the basis for ROI assignment. Count-rate data were extracted from epidermal cells, without distinguishing between trichoblast (root hair) and atrichoblast (non-root hair) cells. Within individual cells, the vacuolar (or cytosolic) ROIs were combined into one ROI (that is, one ROI for each organelle type), because these regions are likely to be connected in three-dimensional space within the cells (Extended Data Fig. 1e). Only structures with smallest linear dimension of at least 5 pixels (that is, substantially larger than the size of the primary beam) were selected as ROIs. For each ROI, the average count rate for each elemental species (counts per second) was obtained from the accumulated images. In the absence of suitably matrix-matched standards, absolute elemental concentrations cannot be determined, but measured elemental ratios for specific subcellular compartments, obtained under identical analytical conditions, can meaningfully be compared within and between samples. To optimize comparability, WT and *sos1* seedlings were grown on the same medium, under identical growth conditions, and went through identical cryo-workflow and analysis with identical instrument settings. Both WT and *sos1* roots were included in each CryoNanoSIMS run. Line-profile data (5 pixels wide) were extracted from the regions highlighted on the image (Extended Data Figs. 2a–d and 3a,d).

Growth conditions for confocal microscopy experiments, complementation and root growth assays

In growth condition 1, seeds were surface-sterilized, sown on plates that contained half-strength MS with 0.8% agar (Roth), stratified at 4 °C in the dark for 2 days and grown vertically in growth chambers at 21 °C at constant light. In growth condition 2, seeds were sown in half-strength MS plates with 1% sucrose in a long-day chamber at 21 °C.

Complementation assay. After 4 days of growth on growth condition 1, seedlings were transferred to half-strength MS plates with 100 mM

NaCl for 4 days and imaged. The primary root length was measured at transfer and after 4 days of growth and the increase in primary root growth was presented as delta primary root growth. For delta primary root growth recovery, the seedlings were transferred for 2 days to half-strength MS plates 8 days after salt stress and measured for root growth on day 10.

Confocal imaging. For the experiment with salt treatment in Fig. 4, 7 days after growth in growth condition 2, the seedlings were transferred to half-strength MS plates with 1% sucrose with 25 mM of NaCl or without NaCl, keeping the same growth conditions for another day. The short-term 25 mM and 100 mM NaCl treatments were done on 4-day-old roots grown in growth condition 1 (without sucrose). Brefeldin A (BFA) and Wortmannin treatments were performed on 7-day-old seedlings grown on growth condition 1 and treatments performed in liquid half-strength MS. BFA treatments were with 25 μM BFA and costained with 2 μM FM4-64 for approximately 1 h before imaging. For the BFA treatment on *SOS1-GFP* lines crossed with VAMP711-mCherry, the seedlings were not costained with FM4-64. Wortmannin treatments were with 33 μM Wortmannin for approximately 1 h before imaging.

Cloning and plasmid construction

For plasmid construct 1, *SOS1-GFP*²⁶ (Extended Data Fig. 5b), a 4.8 kb DNA fragment containing the promoter and the first 13 exons and 13 introns (from -1,929 to +2,964) of the *SOS1* locus, was amplified by polymerase chain reaction (PCR) using *Arabidopsis* genomic DNA as template and primers SOS1proHindIII-fwd (CGGGAAAGCTT ATACGTTTCGTAAGAAC) and SOS1BamHI-rev (AAATTGGGTACTGG ATC). The PCR product was digested and subcloned in pBI321 using *Hind*III and *Bam*HI sites. Next, pGPTV-II-GFP plasmid containing the *SOS1* cDNA was digested at the unique *Bam*HI and *Sac*I sites. A 2.9 kb *Bam*HI/*Sac*I fragment containing the final part of the *SOS1* cDNA fused to GFP was isolated and ligated in frame to the *SOS1* genomic sequence of the pBI321 construct digested with the same restriction enzymes. For plasmid construct 2, *SOS1-mCitrine* (Extended Data Fig. 5c), a 8.357 kb DNA fragment containing the promoter and the full genomic sequence of *SOS1* (from -2,250 to +6,073), was amplified by PCR using *Arabidopsis* genomic DNA as template and primers SOS1-fwd (ACAAAAAAAGCAGGGCT actaggatgtgtgttaatgtgagaggaagaagaa) and SOS1-rev (cccttgctca ccataGATCGTTCCTGAAACGATTTACTCGGAGA). For the mCitrine, a 7.47 kb DNA fragment was amplified by PCR from a pEN-R2-mCitrine-L3 plasmid (pEDO05) and primers mCitrine-fwd (TCAGGAACGATCTAatgg tgagcaaggcgag) and mCitrine-rev (AACATCTCAATTCTCActtgacag ctgcgtcatgc). For the terminator of *SOS1*, a 2.087 kb DNA fragment (from +6,077 to +8,127) was amplified by PCR using *Arabidopsis* genomic DNA as template and primers SOS1t-fwd (cgagctgtacaagTGAGAATTG AGATGTTGTAACATAAGAAAACAAATTGTTAGCT) and SOS1t-rev (CAAGAAAGCTGGGTTactagactgtttatattgtaatttagttgggct). Fragments were assembled by In-Fusion (Takara) into pENTR_L1L2 vector digested with *Bpu*I (pRU335).

Confocal laser-scanning microscopy

Confocal images were acquired using a Leica Stellaris 5 WLL inverted confocal microscope with a $\times 63$ objective with LASX (2022) software. For treatments, 7-day-old *Arabidopsis* seedlings were mounted with 30 μl of the corresponding medium (the same as used for the treatment) and imaged. For propidium iodide (PI) staining, PI was dissolved in liquid Na-free medium (10 μg ml⁻¹ PI) and seedlings were immersed for 3 min, washed and imaged. GFP was excited with the 488 nm laser line of the MaiTai white laser and the emission was detected between 495 and 545 nm. PI and mCherry were excited with the 561 nm and emission was detected between 580 and 680 nm. One-shot images were taken with high-resolution 4,096 × 4,096, zoom $\times 3$, in 8 bit depth, with $\times 4$ line averaging.

Spinning disc confocal microscopy

We used a CSU-W1 Yokogawa spinning disk head fitted to a Nikon Eclipse Ti-E-inverted microscope, equipped with a CFI PlanApo $\times 100$ numerical aperture, 1.40 oil immersion objective and with two EMCCD Andor iXon Ultra, operating with $1,024 \times 1,024$ pixels and $13 \times 13 \mu\text{m}$ pixel size. GFP and RFP or mCherry were excited and detected simultaneously (excitation: GFP 488 nm, RFP/mCherry 561 nm; detection: GFP 525/50 nm; RFP/mCherry ET630/75 nm). Time-lapse images were processed using the in-built plugins of Fiji, that is, background subtraction (rolling ball radius, 30–50 pixels) and walking average projection (3–4 frames averaging) for the images for representative purposes.

Fluorescence signal and vesicle colocalization quantification

For intensity measurement of pixels, the ROIs were defined conservatively for the structures of interest: plasma membrane and internal area of the cell. The raw integrated density values were extracted for the ROIs. For the plasma membrane, the raw integrated density values were multiplied by a correction factor of 0.75 to account for the overlapping plasma membrane between cells and unaccounted cell faces. For the vesicle colocalization, background subtraction was performed using the ‘subtract background’ tool with a rolling ball radius of 50 pixels. The region encompassing a SOS1-GFP vesicle served as the ROI for each colocalization measurement for VHAa-1, RABF2a and RABF2b. A fixed size ROI with signal from mCherry-VAMP711 was used as a reference to quantify colocalization with SOS1-GFP for the vacuolar membranes. Pearson’s *R* values were determined using the Coloc2 plugin in FIJI.

Isolation of intact vacuoles

Protoplasts from leaves of 5-weeks-old *Arabidopsis* plants were isolated following the method described in ref. 37. The solution containing protoplasts was mixed (1:1) with lysis buffer, 200 mM sorbitol, 10% ficoll, 20 mM EDTA, 10 mM HEPES, pH 8.0, to release the vacuoles³⁸.

Arabidopsis membrane isolation and purification

Total microsomes and tonoplast membranes used for western-blot analysis were isolated as described in ref. 39. Leaves were homogenized in a commercial blender and centrifuged at 10,000*g* for 20 min at 4 °C. The supernatant was centrifuged at 80,000*g* for 50 min at 4 °C, to obtain the microsomal fraction. Vacuolar membranes were isolated by loading the microsomal suspension onto a discontinuous sucrose gradient (0/20% w/v) that were centrifuged at 100,000*g* for 3 h at 4 °C.

Affinity purification of antibodies and western blotting

Anti-SOS1 antibodies were affinity purified according to ref. 40. A polypeptide comprising amino acids 998–1146 of *Arabidopsis* SOS1 was expressed and purified from *E.coli* as GST fusion. The protein was subjected to SDS-PAGE and transferred to nitrocellulose paper. After Ponceau S staining, the protein band corresponding to GST-SOS1 was cut out and incubated in TBS-T 5% non-fat milk for 1 h. The nitrocellulose strip was incubated overnight with anti-SOS1 serum⁴¹ diluted 1:1 in TBS. For elution of specifically bound antibodies, the nitrocellulose strip was incubated with 0.2 M glycine-HCl, pH 2.8 and 1 mM EGTA for 2 min. The eluate was neutralized immediately with 1 M Tris base. For western blots, protein samples were separated on 10% polyacrylamide SDS-PAGE gel and then electroblotted onto an Amersham Protran nitrocellulose membrane (Cytiva). The membrane was blocked for 1 h with TBS-T 5% non-fat milk. Then, the membrane was incubated overnight at 4 °C with the primary antibody (purified anti-SOS1 antibodies, 1:2,000 dilution; antiEpsilon subunit of tonoplast H⁺-ATPase antibody AS07213 from Agrisera, 1:10,000 dilution) in TBS-T 5% non-fat milk. Horseradish peroxidase-conjugated goat antimouse secondary antibody was used diluted 1:10,000 in TBS-T. The membrane was washed three times in TBS-T and incubated in ECL Select Western Blotting Detection Reagent

for 5 min. The images were obtained using a GE Amersham Imager Al680 system. Refer to Supplementary Fig. 1 for full blots.

SEM image analysis and figure preparation

The SEM images were processed with levels setting in Photoshop (v.25.11.0). All NanoSIMS images were analysed using the L’IMAGE software v.10-15-2021 developed by L. Nittler. All confocal images were analysed using the ImageJ v.1.54 f (<http://imagej.nih.gov/ij/>)⁴² and Fiji programs. Figures were prepared using Adobe Illustrator (v.28.7.1) and Fiji. The only manipulation of images were histogram adjustments. Figures were then assembled in the Adobe Illustrator and Photoshop programs.

Statistics and reproducibility

We compared the effect of treatment on the two genotypes and considered each organelle separately. We performed two-way analysis of variance (ANOVA) and a paired comparison with treatment and genotype as the two factors, and significant interactions were determined by post hoc Tukey test for vacuole:cytosol ratio and Na:K ratio. Box plots for ratios show the mean with standard deviation and standard error. For Fig. 1b,c, the images are representative illustrations of a cryo-planed root meristem and elemental distribution performed on three different roots. The data for Fig. 2d,e were obtained using the following. Na-free medium: WT *n* = 15 cells; *sos1* *n* = 13 cells, from one experiment with three different roots. 25 mM NaCl treatment: WT *n* = 49 cells; *sos1* *n* = 33 cells, from two experiments with six roots in total. Pairwise comparison of vacuole:cytoplasm ratio was carried out with treatment and genotype as factors; Na-free medium: WT *n* = 15 cells; *sos1* *n* = 13 cells, from one experiment with three different roots. 25 mM NaCl treatment: WT *n* = 22 cells; *sos1* *n* = 23 cells, from two experiments with six roots in total. Significance: *** *P* < 0.001 analysed by two-way ANOVA with Tukey post hoc tests. The data for Fig. 3b,c were obtained using the following 100 mM NaCl treatment: WT *n* = 34 cells; *sos1*, *n* = 26 cells from two experiments with six roots in total. Box plots show the mean values (horizontal lines), 25% (boxes) and 75% (thin vertical bars) quartiles; outliers are indicated with solid circles. Pairwise comparison of ratios was carried out with treatment and genotype as factors. Significance: ****P* < 0.001 analysed by two-way ANOVA with Tukey post hoc tests. For Fig. 3d, rice root meristems were treated with 100 mM NaCl, WT *n* = 18 cells. Statistical analyses were performed using OriginPro v.2023b and GraphPad software (Prism 10). Figure 4a is a representative picture of *n* = 7 roots with three biological replicates.

Reporting summary

Further information on research design is available in the Nature Portfolio Reporting Summary linked to this article.

Data availability

All associated pre-processed and processed data for the CryoNanoSIMS and fluorescence images are available at Zenodo (<https://doi.org/10.5281/zenodo.14054006>)⁴³. Full versions of all gels and blots presented are provided in Supplementary Fig. 1. Source data are provided with this paper.

36. Dettmer, J., Hong-Hermesdorf, A., Stierhof, Y.-D. & Schumacher, K. Vacuolar H⁺-ATPase activity is required for endocytic and secretory trafficking in *Arabidopsis*. *Plant Cell* **18**, 715–730 (2006).
37. Wu, F.-H. et al. Tape-*Arabidopsis* Sandwich - a simpler *Arabidopsis* protoplast isolation method. *Plant Methods* **5**, 16 (2009).
38. Schneider, S. et al. Vacuoles release sucrose via tonoplast-localised SUC4-type transporters. *Plant Biol.* **14**, 325–336 (2012).
39. Vera-Estrella, R., Barkla, B. J., Garcia-Ramirez, L. & Pantoja, O. Salt stress in *Thellungiella halophila* activates Na⁺ transport mechanisms required for salinity tolerance. *Plant Physiol.* **139**, 1507–1517 (2005).
40. Sambrook, J. *Molecular Cloning: A Laboratory Manual*, Vol. 3 (Cold Spring Harbor Laboratory, 1989).

41. Núñez-Ramírez, R. et al. Structural insights on the plant salt-overly-sensitive 1 (SOS1) Na⁺/H⁺ antiporter. *J. Mol. Biol.* **424**, 283–294 (2012).
42. Rasband, W. S. ImageJ v.1.54f (NIH, 2023).
43. Ramakrishna, P. et al. Data for “SOS1-dependent vacuolar sodium accumulation revealed by elemental cryo-imaging”. Zenodo <https://doi.org/10.5281/zenodo.14054006> (2024).
44. Hallgren, J. et al. DeepTMHMM predicts alpha and beta transmembrane proteins using deep neural networks. Preprint at *bioRxiv* <https://doi.org/10.1101/2022.04.08.487609> (2022).

Acknowledgements We thank F. Plane, A. Mucciolo and J. Daraspe for technical advice and assistance. We thank D. Salt for critical comments on the manuscript. We thank the Central Imaging Facility of the University of Lausanne and the Scientific Center for Optical and Electron Microscopy (ScopeM, ETH Zurich) for technical support. This work was supported by grant PID2022-140705OB-I00 (AEI-MCIN, Spain, co-financed by ERDF) to F.J.Q., and by in-house funding from ETH Zurich to C.S.-R., from the University of Lausanne to N.G. and from EPFL to A.M. The development of the CryoNanoSIMS was funded by EPFL, the University of Lausanne, grants from the Swiss National Science Foundation (206021_150762, 200021_179092 and 205321_212614) and a European Research Council Advanced Grant 246749 to A.M.

Author contributions P.R., N.G. and A.M. conceived, designed and coordinated the CryoNanoSIMS project. P.R., C.M.-O., D.D.B. and C.G. contributed to the cryo-sample preparation and analyses. P.R., S.E. and A.M. carried out CryoNanoSIMS analyses. N.G., P.R. and C.S.-R. designed and coordinated mutant analysis, stress treatments and protein localization work. F.M.G.-A. and E.B. contributed equally to the protein work and analyses. P.R., F.M.G.-A., E.B., A.D.L., J.M.P., F.J.Q., C.S.-R. and N.G. contributed to the protein localization work and interpretation of the results. P.R., N.G. and A.M. wrote the first draft of the manuscript. All authors contributed to the final version of the manuscript.

Competing interests The authors declare no competing interests.

Additional information

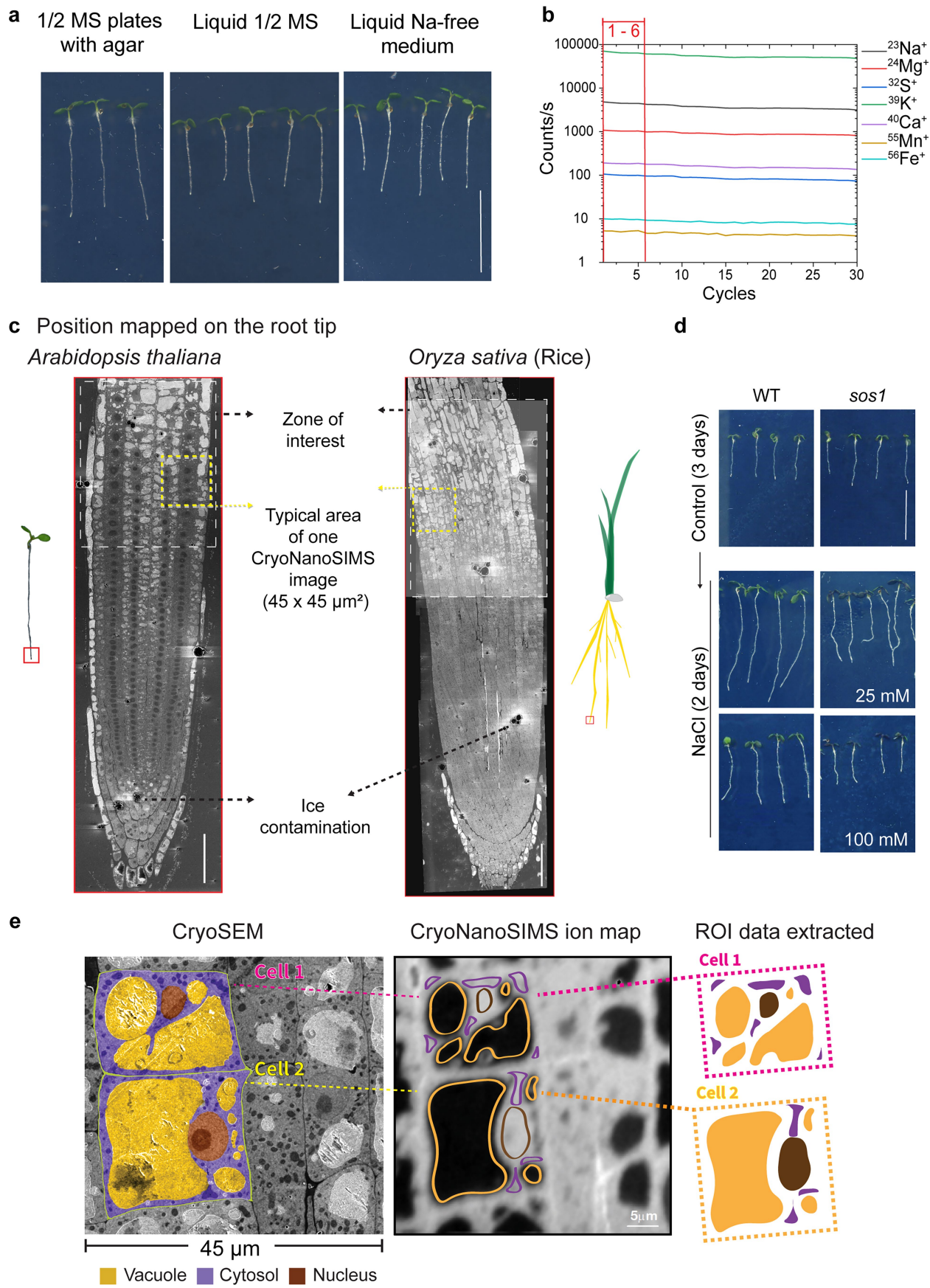
Supplementary information The online version contains supplementary material available at <https://doi.org/10.1038/s41586-024-08403-y>.

Correspondence and requests for materials should be addressed to Priya Ramakrishna, Niko Geldner or Anders Meibom.

Peer review information *Nature* thanks Nobuyuki Uozumi, Christa Testerink and the other, anonymous, reviewer(s) for their contribution to the peer review of this work. Peer reviewer reports are available.

Reprints and permissions information is available at <http://www.nature.com/reprints>.

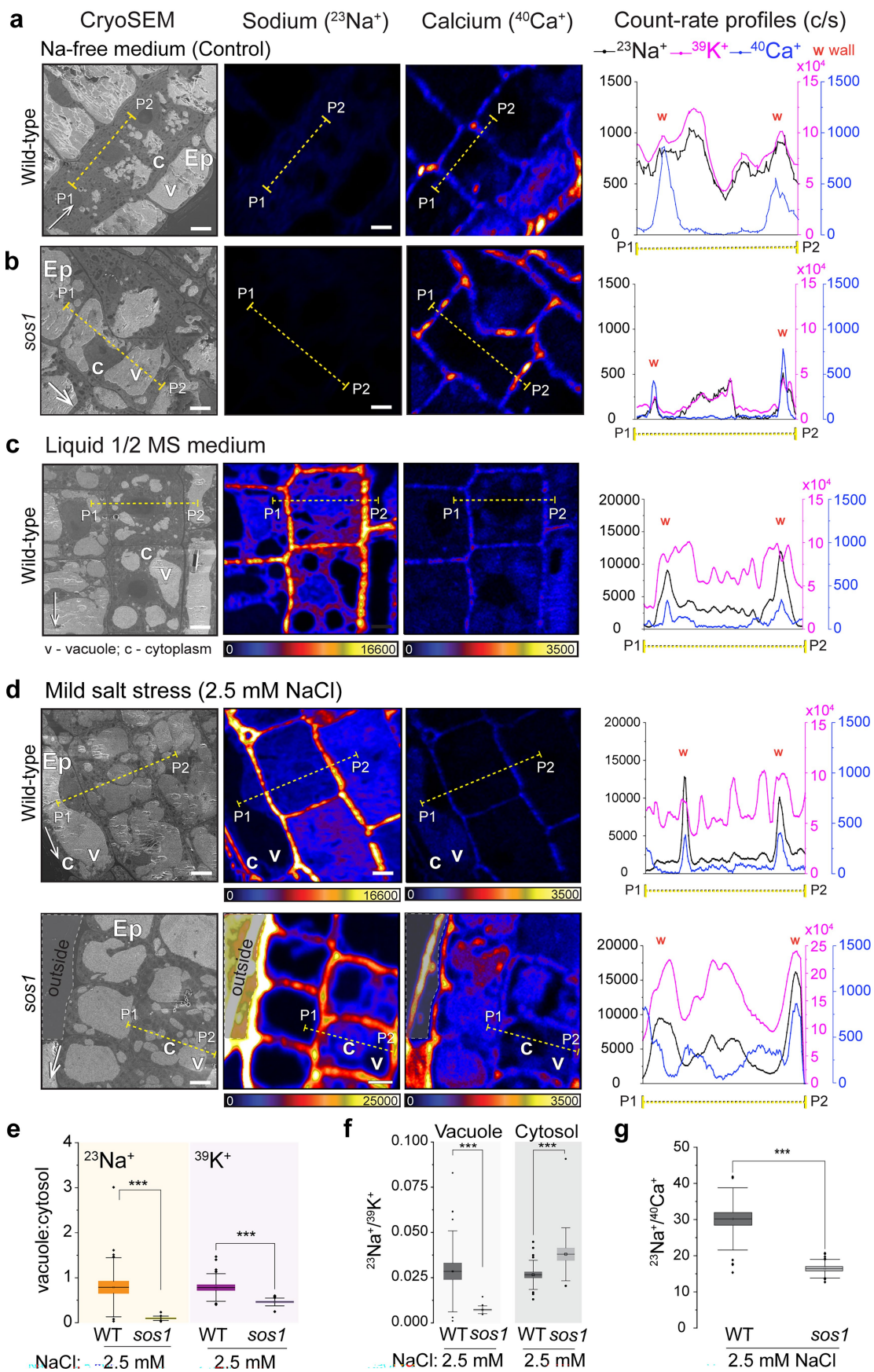
Article



Extended Data Fig. 1 | See next page for caption.

Extended Data Fig. 1 | Supporting documentation of experiments and the correlated cryoSEM and CryoNanoSIMS workflow. **a.** Comparison of 5-day old WT *Arabidopsis* seedlings grown on half-strength MS plates versus the hydroponic system with liquid half-strength MS, or Na-free media, demonstrating that growth rates were similar. For easy comparison, the seedlings from the hydroponics system were transferred to an agar surface and immediately imaged. **b.** Plot showing CryoNanoSIMS count rates of $^{23}\text{Na}^+$, $^{24}\text{Mg}^+$, $^{32}\text{S}^+$, $^{39}\text{K}^+$, $^{40}\text{Ca}^+$, $^{55}\text{Mn}^+$ and $^{56}\text{Fe}^+$ from a representative $45 \times 45 \mu\text{m}^2$ area on a vitrified WT root, similar to that indicated in (c). Note that the count rates are stable for (more than) 30 image cycles. For the data reported in this study, 6 image cycles were systematically acquired in each imaged area of the roots. This was enough to obtain sufficient counting statistics in all regions of interest. **c.** Representative block face cryoSEM image of a high-pressure frozen and vitrified *Arabidopsis* and rice (*Oryza sativa*) root tip processed with the cryogenic workflow (also refer to Fig. 1). The dotted yellow boxes each frame an area of $45 \times 45 \mu\text{m}^2$ on the sample, the size of a typical CryoNanoSIMS image in this study. The larger white shaded rectangle indicates the general root-zone

systematically mapped with the CryoNanoSIMS in each the root tip to ensure comparison of the same cell types in similar stage of development, here the region in which the cells transition from division to elongation. **d.** Reduced root growth in response to salt stress in *sos1* *Arabidopsis* compared to WT with increasing salt concentrations. Five-day old WT and *sos1* seedlings were grown for 3 days (control) on half-strength MS agar plates and exposed to salt concentrations of 25 and 100 mM respectively for two days. **e.** Left: A representative cryoSEM image of *Arabidopsis* root meristem cells annotated with regions of interest (ROIs) representing vacuoles (yellow), cytosol (purple) and nucleus (with nucleolus) (brown). These SEM images served to assign ROIs on the CryoNanoSIMS images. Middle: Correlated CryoNanoSIMS ion map with similar ROI definitions from which average count-rates of the measured ions were obtained using the L'IMAGE software. Within individual cells, the vacuole areas were treated as one single ROI, and the cytosol areas as one single ROI, which were then used to derive the average vacuole:cytosol ratio for each cell, as indicated on the right. Scale bars, 1 cm (**a, d**), $45 \mu\text{m}$ (**c**).

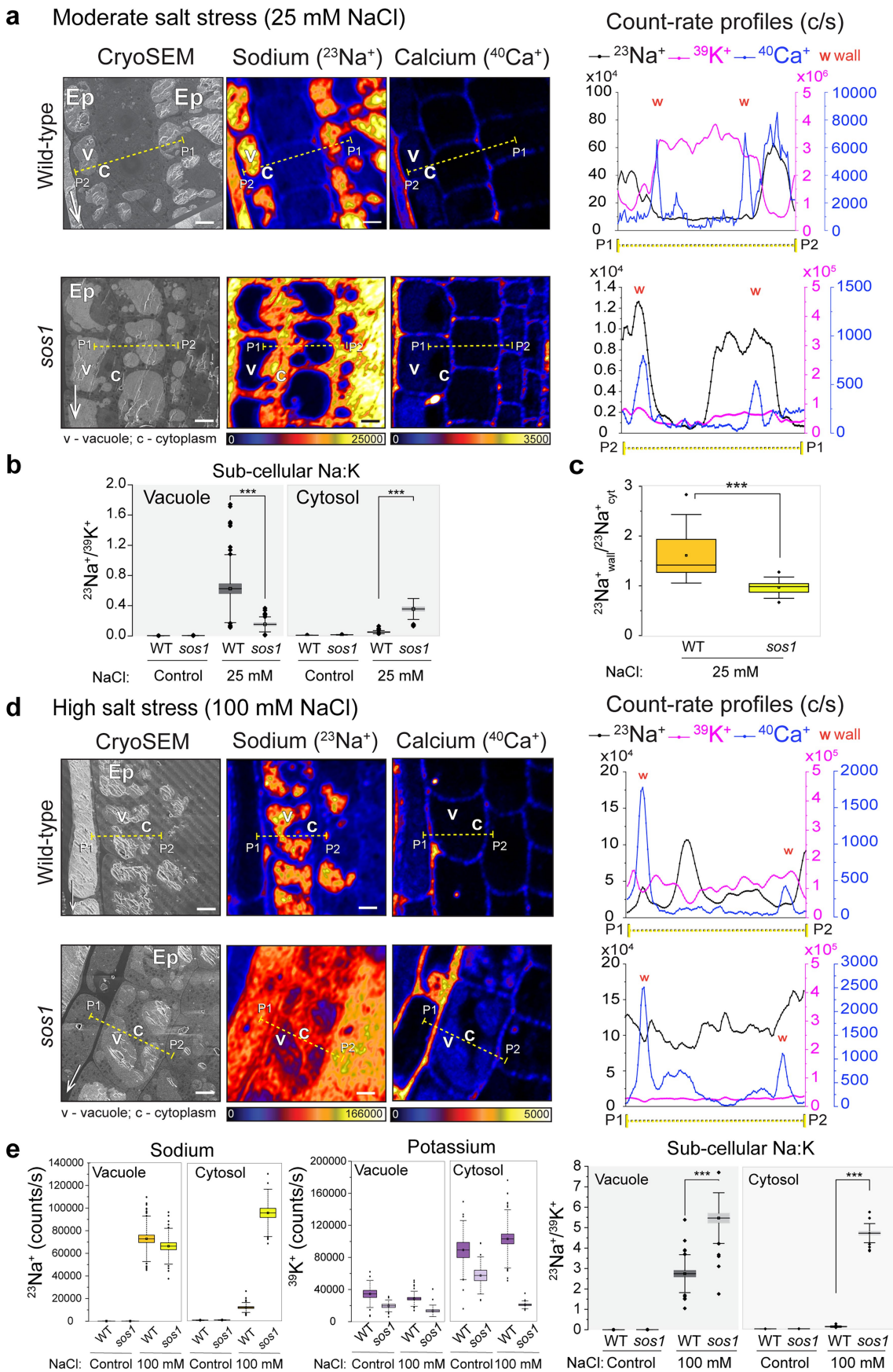


Extended Data Fig. 2 | See next page for caption.

Extended Data Fig. 2 | CryoNanoSIMS mapping of sub-cellular Na, K and Ca accumulation in the *Arabidopsis* root meristem grown on different media.

Correlated SEM images and elemental maps of $^{23}\text{Na}^+$ and $^{40}\text{Ca}^+$ from roots of seedlings grown in the hydroponics set-up. To the right are extracted line profiles as indicated on the CryoNanoSIMS maps. The line profiles show count rate profiles for $^{23}\text{Na}^+$, $^{39}\text{K}^+$ and $^{40}\text{Ca}^+$ spanning two cell walls, marked with 'W'. Note that Ca is strongly concentrated in the cell walls. **a-b.** WT (a) and *sos1* (b) seedlings grown on Na-free medium. Note that, even in seedlings grown on the Na-free medium (control), the cellular Na concentrations permit clear detection by the CryoNanoSIMS, testifying to the high sensitivity of the instrument for these elements. Epidermis (Ep), vacuole (v) and cytoplasm (c) are labelled. **c.** WT seedlings grown on liquid half-strength MS for 5 days. Na is concentrated in cell walls in the root meristem cells. **d.** Under mild Na-stress (2.5 mM NaCl) for 2 h, Na remains concentrated in the cell walls of root meristem cells in both WT and *sos1*. **e.** Vacuole:cytosol count rate ratios of $^{23}\text{Na}^+$ and $^{39}\text{K}^+$ within individual meristem cells in wild-type and *sos1* after treatment with 2.5 mM NaCl for 2 h. **f.** Average $^{23}\text{Na}^+/\text{Na}^+$ ratios measured in vacuoles and cytosol within meristem

cells in WT and *sos1* seedlings grown on Na-free media and after treatment with 2.5 mM NaCl for 2 h. **g.** Average $^{23}\text{Na}^+/\text{Na}^+$ ratios measured in the cell walls of WT and *sos1* seedlings after treatment with 2.5 mM NaCl for 2 h. Line-profiles are 5 pixels wide and representative of image and position highlighted. For Na-free medium: WT $n = 15$ cells; *sos1* $n = 13$ cells, from one experiment with three different roots. For liquid half-strength MS, WT $n = 14$ cells from two experiments with two different roots. For the 2.5 mM NaCl treatment: WT $n = 24$ cells; *sos1* $n = 18$ cells, from one experiment with three different roots. For (g), WT $n = 24$; *sos1* $n = 18$. Box plots show the mean values (horizontal lines), 25% (boxes) and 75% (thin vertical bars) quartiles; outliers are indicated with solid circles. Pairwise comparison of ratio with treatment and genotype as factors. Significance: *** $P < 0.001$ analysed by two-way ANOVA with Tukey post hoc tests. The sample were hydroponically grown on a Na-free medium and subject to respective treatments. Colour scales are linear and maximum ion count rates (counts per second) are indicated by the colour bars. Thin white arrows in cryoSEM images point towards the root tip. Scale bars, 5 μm .

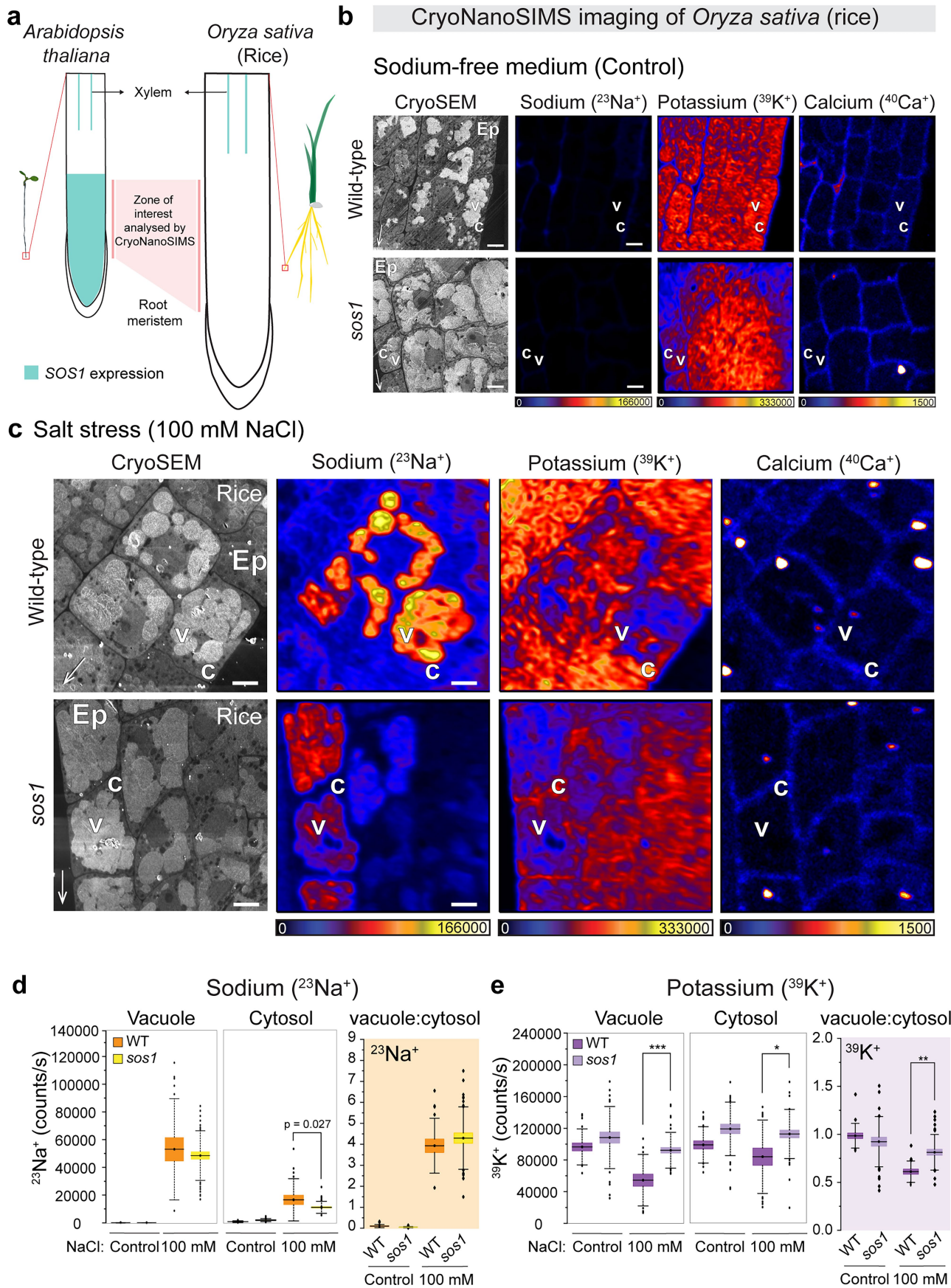


Extended Data Fig. 3 | See next page for caption.

Extended Data Fig. 3 | Supporting data for mapping of Na, K, and Ca in root meristems of *Arabidopsis* WT and *sos1* mutants under moderate and high salt stress. **a.** Correlated SEM image and isotope maps of $^{23}\text{Na}^+$, and $^{40}\text{Ca}^+$ from roots of WT and *sos1* seedlings grown on 25 mM NaCl for 4 hrs, with corresponding count rate profiles across two cell walls, including also $^{39}\text{K}^+$ (right). **b.** Ratios of average count rates of $^{23}\text{Na}^+$ and $^{39}\text{K}^+$ in vacuole and cytosol of root meristematic epidermal cells of WT and *sos1* seedlings grown on Na-free media, and after treatment with 25 mM NaCl for 4 h. **c.** $^{23}\text{Na}^+$ wall-to-cytosol ratios in root meristem epidermal cells of WT and *sos1* seedlings after treatment with 25 mM NaCl for 4 h. **d.** Correlated SEM image and isotope maps of $^{23}\text{Na}^+$, and $^{40}\text{Ca}^+$ from roots of WT and *sos1* seedlings grown on 100 mM NaCl for 4 hrs, with corresponding count rate profiles across two cell walls, including also $^{39}\text{K}^+$ (right). **e.** Average count rates (counts per second) of $^{23}\text{Na}^+$ (left) and $^{39}\text{K}^+$ (middle) in vacuoles and cytosol of WT and *sos1* seedlings grown on Na-free media, and post treatment with 100 mM NaCl for 4 h. Right: Ratios of $^{23}\text{Na}^+$ and $^{39}\text{K}^+$ count rates in vacuole and cytosol of root meristem epidermal cells of WT and *sos1*

seedlings grown on Na-free media, and after treatment with 100 mM NaCl for 4 h. Count rate profile plots show the average count rate for sodium, potassium and calcium for the line-profiles highlighted on the corresponding images. Line-profile data are 5 pixels wide. For the Na-free medium: WT $n = 15$ cells; *sos1* $n = 13$ cells, from one experiment with three different roots. For 25 mM NaCl treatment (a-c): WT $n = 49$ cells; *sos1* $n = 33$ cells, from two experiments with three different roots. For the 100 mM NaCl treatment (d,e): WT $n = 34$ cells; *sos1*, $n = 26$ cells from two experiments with three different roots. Box plots show the mean values (horizontal lines), 25% (boxes) and 75% (thin vertical bars) quartiles; outliers are indicated with solid circles. Pairwise comparison of vacuole:cytosol ratios with treatment and genotype as factors. Significance: *** $P < 0.001$ analysed by two-way ANOVA with Tukey post hoc tests. Colour scales are linear and maximum ion count rates (counts per second) are indicated by the colour bars. Thin white arrows in cryoSEM images point towards the root tip. Scale bars, 5 μm .

Article

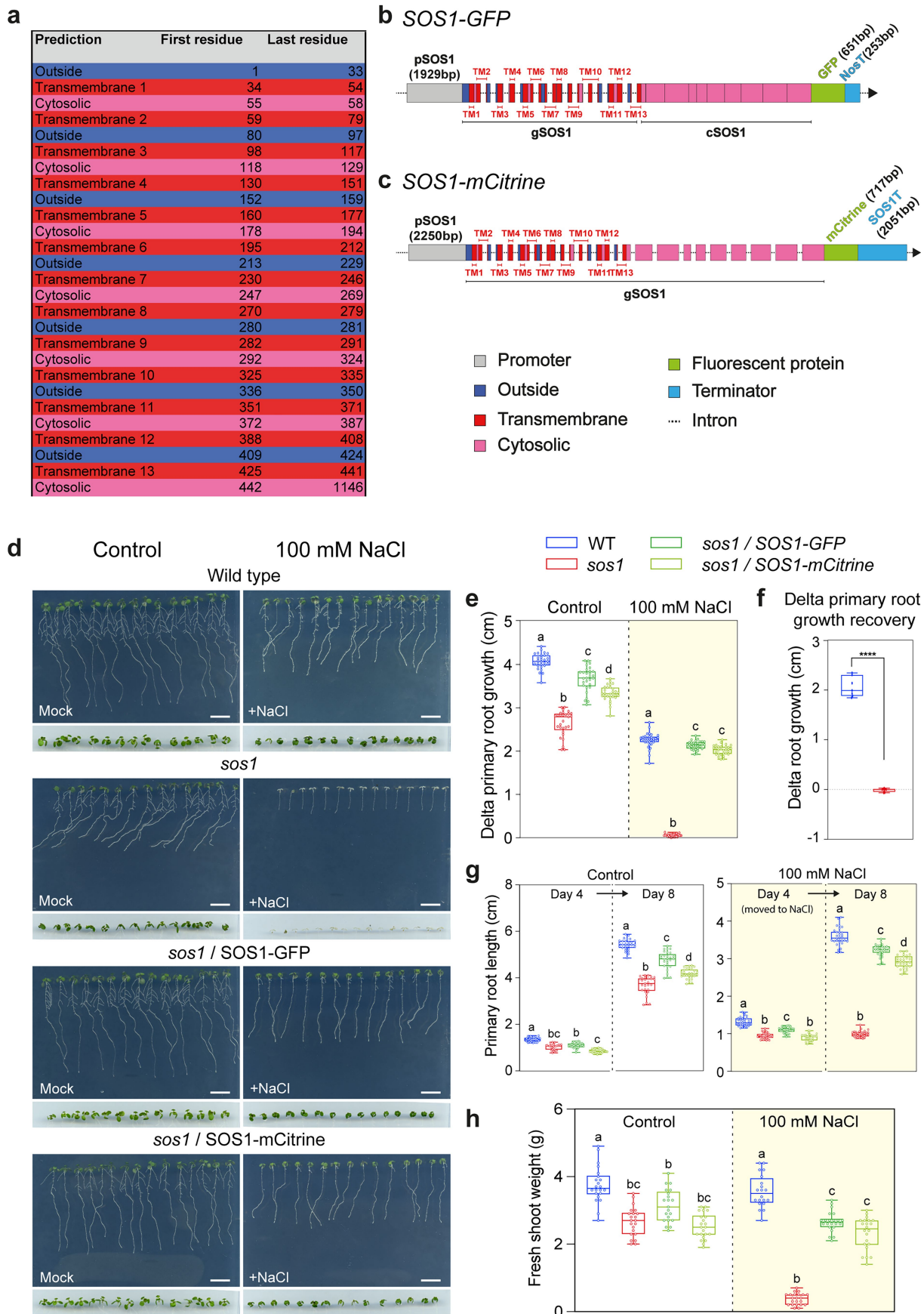


Extended Data Fig. 4 | See next page for caption.

Extended Data Fig. 4 | Correlative cryoSEM-CryoNanoSIMS mapping of subcellular Na, K and Ca distribution in rice root meristem. **a.** Schematic of previously described *SOS1* gene expression pattern in *Arabidopsis*¹⁹ and rice (*Oryza sativa*)²² with the zone of interest analysed by CryoNanoSIMS highlighted. **b.** WT and *sos1* rice seedlings grown in a Na-free media (control), characterized by very low, but clearly measurable, background Na levels prior to salt stress experiments. Epidermis (Ep), vacuole (v) and cytoplasm (c) are labelled. **c.** Root meristem of WT and *sos1* rice seedlings subject to salt stress by treatment with 100 mM NaCl for 4 h. Note, in rice where *SOS1* is not expressed in the root meristem, Na accumulates in the vacuole of *sos1* similar to WT. **d.** Average count rates for sodium (²³Na⁺) in the vacuole and cytosol of the rice root meristem cells in WT and *sos1* (left) after growth in Na-free medium (control) and after treatment with 100 mM NaCl for 4 h. Vacuole:cytosol count rate ratios of ²³Na⁺ within individual meristem cells in WT and *sos1* (right, orange). **e.** Corresponding

average count rates for potassium (³⁹K⁺) in the vacuole and cytosol of the meristem cells in WT and *sos1* (left). Vacuole:cytosol count rate ratios of ³⁹K⁺ within individual meristem cells in WT and *sos1* after growth (right, lilac). For Na-free medium (**b,d,e**): WT $n = 20$ cells; *sos1* $n = 31$ cells, from one experiment with at least two different roots. For **c-e** 100 mM NaCl treatment (**c-e**): WT $n = 18$ cells; *sos1* $n = 40$ cells, from two experiments with total five roots. Box plots show the mean values (horizontal lines), 25% (boxes) and 75% (thin vertical bars) quartiles; outliers are indicated with solid circles. Pairwise comparison of ratios with treatment and genotype as factors. Significance: * $P < 0.05$; ** $P < 0.01$; *** $P < 0.001$ analysed by two-way ANOVA with Tukey post hoc tests. Colour scales are linear and maximum ion count rates (counts per second) are indicated by the colour bars. Thin white arrows in cryoSEM images point towards the root tip. Scale bars, 5 μm .

Article

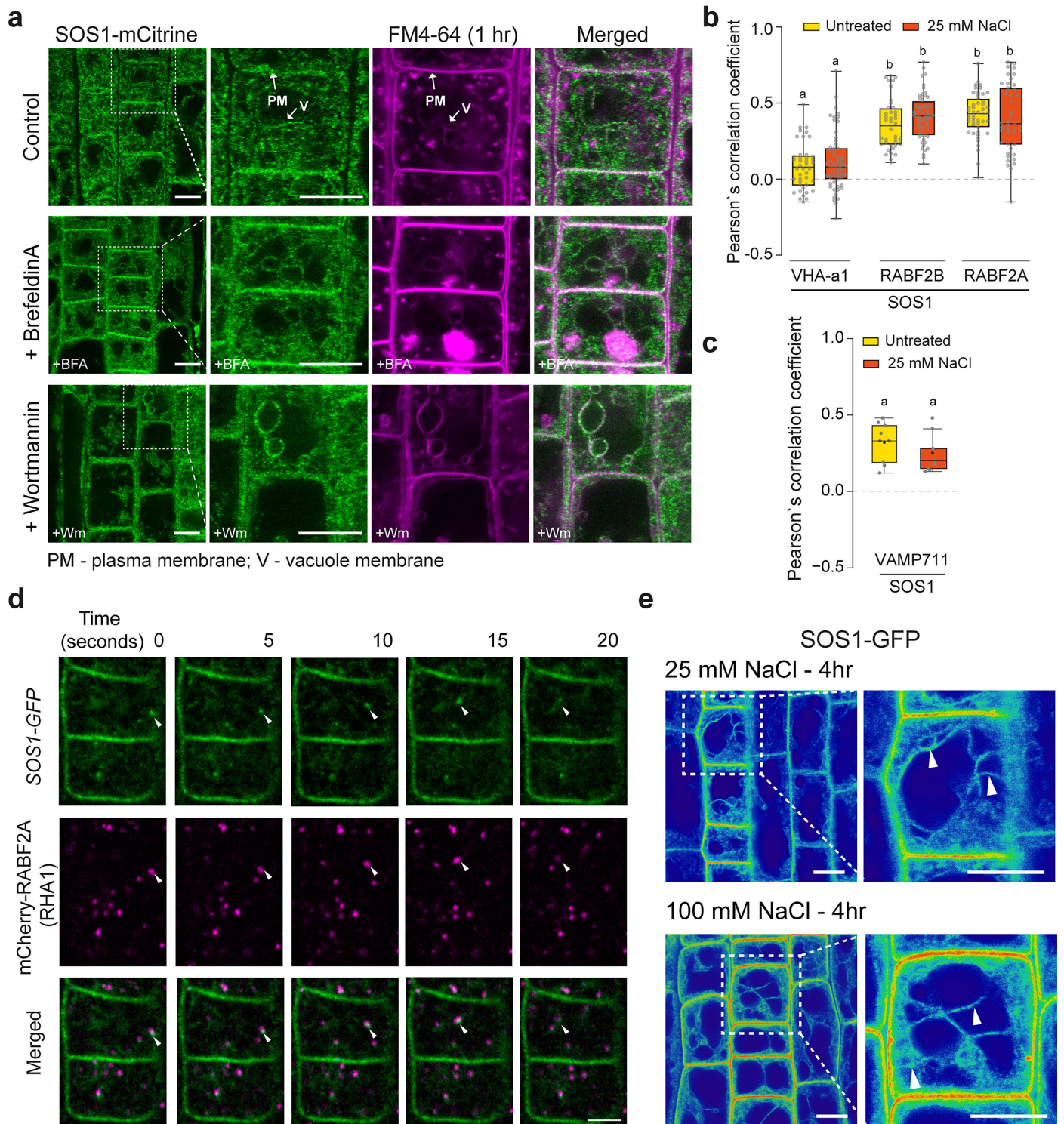


Extended Data Fig. 5 | See next page for caption.

Extended Data Fig. 5 | Arabidopsis SOS1 protein structure and domains and complementation of SOS1 protein. **a.** Table of the topology prediction for SOS1 protein. The residues presented take into account the amino acid sequence from UniProt database (Q9LK9, AT2GO1980) and prediction is based on DeepTMHMM⁴⁴. Colours correspond to structure presented in (b) and (c). **b.** Schematic of the genomic construct 1 (*SOS1-GFP*) used for all the analyses. *SOS1* promoter region (*pSOS1*) corresponded to 1929 bp upstream from the START codon. Only the first 13 introns were used and the GFP was fused without a linker. Nopaline synthase (*NosT*) from *Agrobacterium tumefaciens* was used as terminator. Colours indicate the predicted protein topology of the corresponding nucleotides. Box size of the exons are scaled to each other according to their number of nucleotides. Box size of promoter and introns are not scaled. The length (in nucleotides) of the promoters, fluorescent proteins and terminators are indicated on the figure. **c.** Schematic of genomic construct 2 (*SOS1-mCitrine*) used for comparative analyses with construct 1. *SOS1* promoter region (*pSOS1*) corresponded to 2250 bp upstream from the START codon. A full genomic DNA sequence of *SOS1* was used that included all introns with the mCitrine fused in without a linker. The endogenous terminator (*SOS1T*) was used that corresponded to 2051 bp downstream from the STOP codon. **d.** Representative images of 8 day old *Arabidopsis* seedlings grown on half-strength MS agar medium for 4 days before transfer to half-strength MS agar without (control) or with 100 mM NaCl for 4 additional days. WT, *sos1*, *sos1* complemented with *SOS1-GFP*, *sos1* complemented with *SOS1-mCitrine* are

shown. Presented also, the close-up of shoot biomass of the corresponding lines at 8 days old. **e.** Delta primary root growth of the indicated *Arabidopsis* lines after 4 days of growth on half-strength MS (control) or half-strength MS supplemented with 100 mM NaCl. **f.** Delta primary root growth recovery of indicated *Arabidopsis* lines 2 days after transfer to half-strength MS plates (mock) once they grew for 4 days on half-strength MS (mock) plus 4 days on half-strength MS supplemented with 100 mM NaCl (yellow). **g.** Primary root length of the indicated *Arabidopsis* lines on control at (day 4) and after 4 days of growth (day 8) (left panel); on 100 mM NaCl right after transfer (day 4) and after 4 days of growth (day 8) (right panel, yellow). **h.** Fresh shoot weight of 8 day-old seedlings treated as indicated in (g). Seedlings were grown on growth condition 1 for all these tests and with respective treatments. Box-plots in **e-g** show primary root length measurements on control and post-transfer to 100 mM NaCl treatment for 5 days. For (e) control: WT $n = 28$, *sos1* $n = 28$, *SOS1-GFP/sos1* $n = 28$, *SOS1-mCitrine/sos1* $n = 29$; For treatment with 100 mM NaCl: WT $n = 31$, *sos1* $n = 29$, *SOS1-GFP/sos1* $n = 29$, *SOS1-mCitrine/sos1* $n = 29$. For (g) control and 100 mM NaCl: WT $n = 29$, *sos1* $n = 29$, *SOS1-GFP/sos1* $n = 29$, *SOS1-mCitrine/sos1* $n = 30$ from three independent experiments. Box plots show the mean values (horizontal lines), 25% (boxes) and 75% (thin vertical bars) quartiles. A two-way ANOVA multiple-comparison with Tukey correction was performed for all except (c) where an unpaired t-test has been applied. Different letters represents difference for which $P < 0.001$. Scale bars, 1 cm.

Article



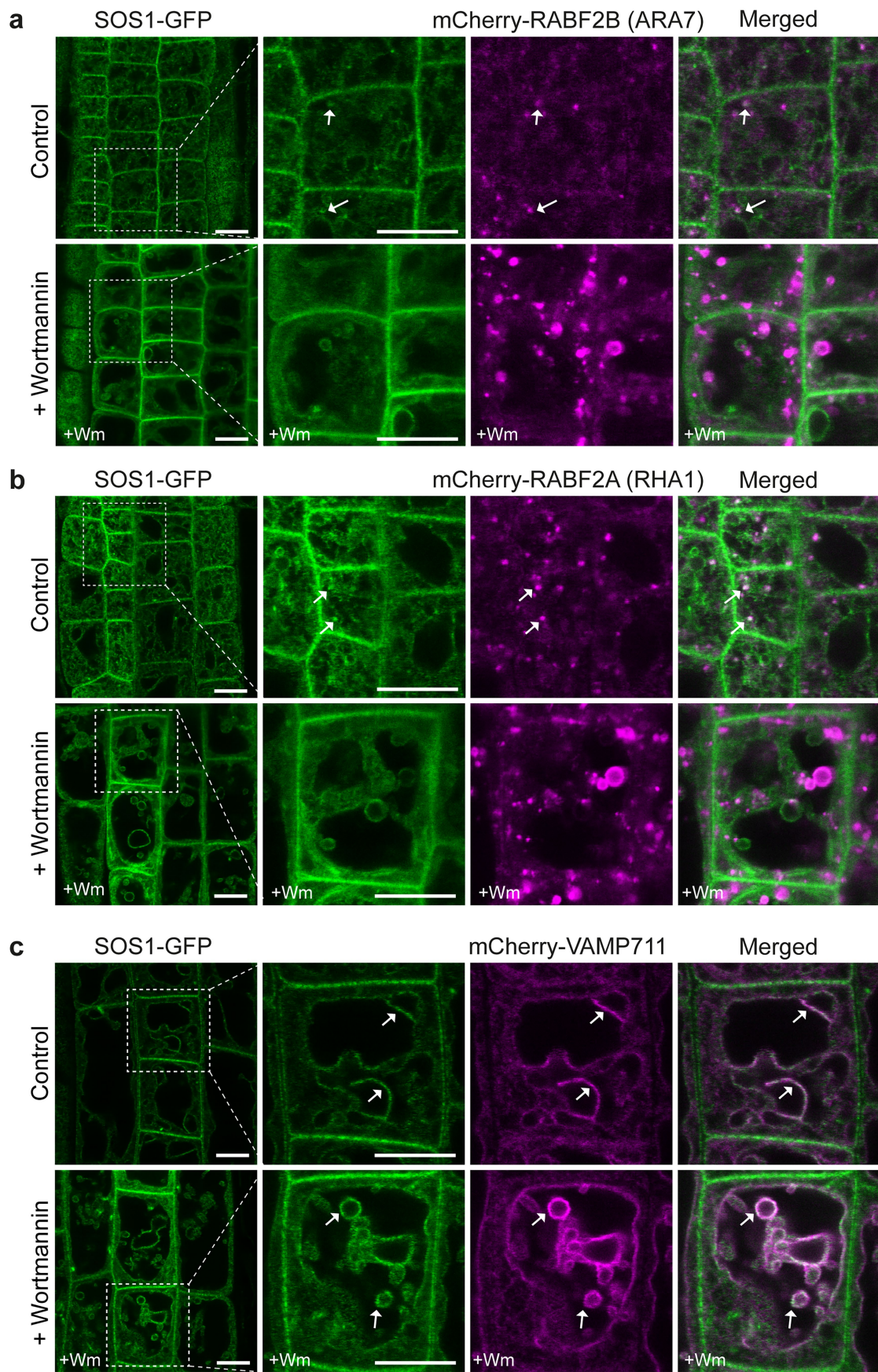
Extended Data Fig. 6 | See next page for caption.

Extended Data Fig. 6 | Subcellular localization of SOS1 protein and association with endomembrane trafficking markers in *Arabidopsis*.

a. Representative picture of subcellular localization of SOS1-mCitrine in root meristems of 7 days old seedlings. Late endosome – prevacuoles and tonoplast highlighted by an arrow, and observed upon Brefeldin A (BFA, 25 μ M) and Wortmannin (33 μ M for about 1 h) treatment. Seedlings were grown on growth condition 1. All seedlings were treated with the fluorescent lipophilic dye FM4-64 (2 μ M), for about 1 h before imaging. **b.** SOS1 colocalization analysis. Association of SOS1-GFP proteins with the early-endosome/trans-Golgi-network marker VHA-a1, and the late-endosome/pre-vacuolar compartments markers RABF2A (RHA1) or RABF2B (ARA7) as shown by Pearson's correlation coefficient. **c.** SOS1-GFP colocalization with vacuolar and endomembrane compartments in mCherry-VAMP711. **d.** Stills from time series of spinning disc video shows the dynamic behaviour of SOS1-GFP (green), and the endomembrane marker

RABF2A (magenta), associated vesicles (white arrows) under control conditions; Also refer to Supplementary Video S2. Seedlings grown on growth condition 2. **e.** Representative images of SOS1-GFP seedlings treated with 25 and 100 mM NaCl for 4 hrs. Seedlings were grown on growth condition 1. For control + FM4-64 treatment (**a**, row one) $n = 7$ roots; BFA + FM4-64 treatments (**a**, row two) $n = 11$ roots; Wortmannin + FM4-64 treatments (**a**, row 3) $n = 9$. All from three independent experiments. For (**b**), $n = 40$ vesicles from 26 cells from six plants and three independent experiments; for (**c**) fixed ROIs from $n = 9$ cells from three plants. Different letters indicate statistically significant differences, $P \leq 0.05$, based on one-way ANOVA and Tukeys multiple comparison test. For (**e**), 25 mM NaCl, 4 h $n = 8$ roots; 100 mM NaCl 4 h, $n = 13$. Box plots: centerlines show the medians; box limits indicate the 25th and 75th percentiles; whiskers extend to the minimum and maximum. Scale bars, 20 μ m (a, e (overview)), 10 μ m (a, e (inset)), 5 μ m (d).

Article

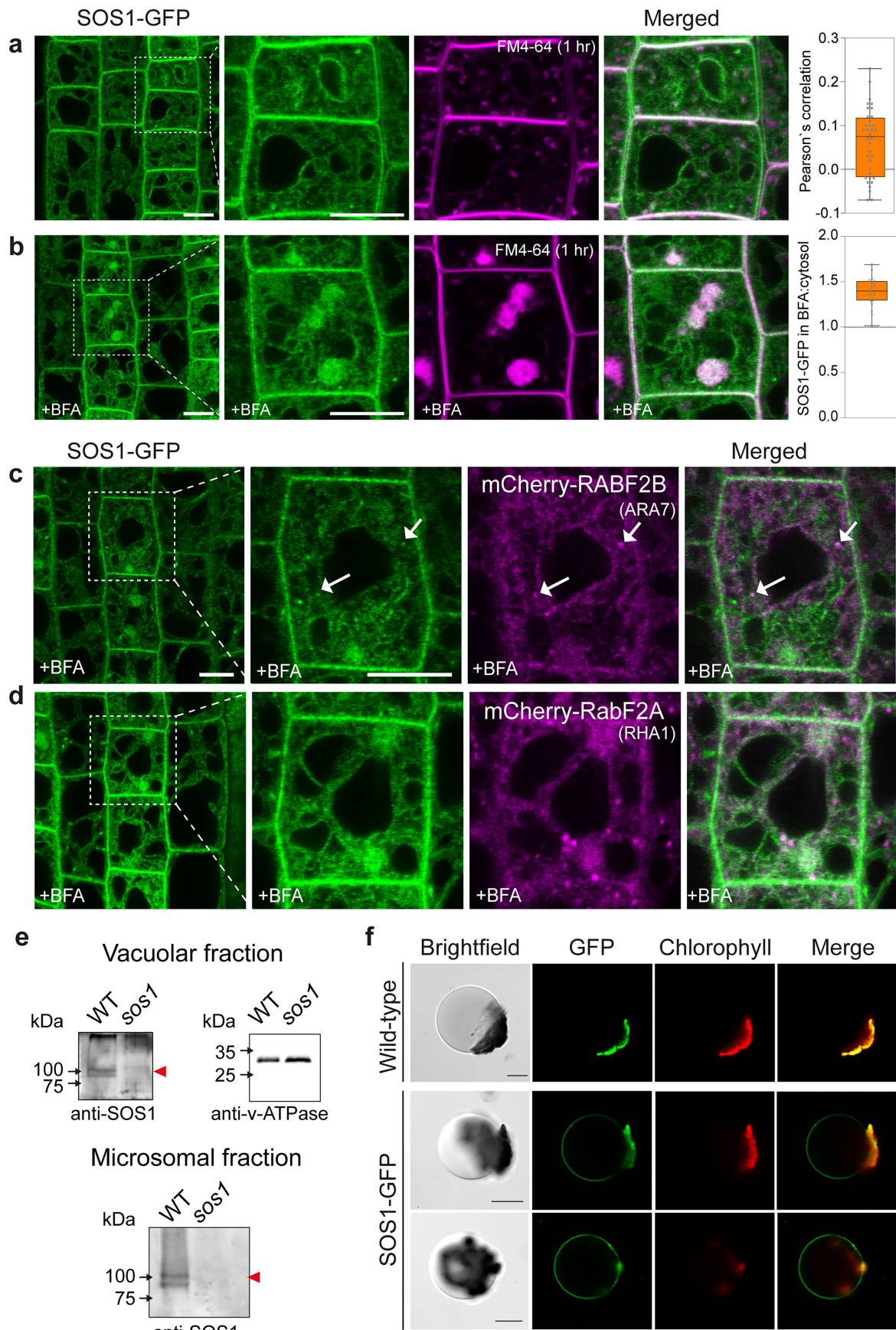


Extended Data Fig. 7 | SOS1-GFP colocalized with RABF2A and RABF2B in swollen Wortmannin-induced prevacuolar structures in *Arabidopsis*.

a-b. Partial association of SOS1-GFP was observed with late endosomal/pre-vacuolar markers mCherry-RABF2B (ARA7) (**a**) and mCherry-RABF2A (RHA1) (**b**), under untreated (control) conditions and was distinct upon Wortmannin (Wm) treatment. Arrows show representative points. **c.** Strong colocalization of SOS1-GFP with mCherry-VAMP711 was induced by Wm treatment, confirming

that a significant part of SOS1-GFP positive endomembrane compartments were vacuolar and prevacuolar compartments. Observable under both untreated (control) and Wm treatment conditions. Seedlings were grown on growth condition 1. For (**a**) control $n=5$ roots, Wm treatments $n=5$ roots; For (**b**) control $n=7$ roots, Wm treatments, $n=5$ roots; For (**c**) control $n=20$ roots, Wm treatments $n=5$ roots. Seedlings were treated with $33 \mu\text{M}$ Wm for about 1 h. Scale bars, $20 \mu\text{m}$ (overview), $10 \mu\text{m}$ (inset).

Article



Extended Data Fig. 8 | See next page for caption.

Extended Data Fig. 8 | Weak accumulation of SOS1-GFP in BFA bodies and detection of SOS1-GFP in vacuolar compartment of *Arabidopsis* leaf tissue.

a. Localization of SOS1-GFP in root epidermal cells in *sos1* complemented lines. Uptake of FM4-64 (2 μM) (magenta) after about 1 h, broadly highlighting early-to-late endosomal compartments. Close-up view of an epidermal cell and overlay (area marked with dotted box). Note: The quantification to show the lack of co-localization between FM4-64 and SOS1-GFP inside the cell. **b.** Brefeldin A (BFA) treatment led to partial accumulation of SOS1 in BFA compartments, with little effect on overall SOS1 localization at other endomembrane compartments or plasma membrane. FM4-64 positive compartments displayed strong aggregation into the BFA compartment. Seedlings were treated with 25 μM BFA and co-stained with FM4-64 for about 1 h. On the right, quantification for the BFA bodies with SOS1-GFP. **c-d.** BFA treatment led to weak accumulation of SOS1 with RABF2B (ARA7) (**c**), and RABF2A (RHA1) (**d**) in the BFA compartments. **e.** Western blot of vacuolar and microsomal fractions of leaf tissue of WT and *sos1* analyzed using a affinity purified anti-SOS1 polyclonal antibody with SOS1

(red arrow), detected in the vacuolar fraction. The vacuole marker v-ATPase was detected using commercial antibodies. Blots are representative of two biological replicates. Refer to Supplementary Fig. 1 for original blots. **f.** SOS1-GFP localization to the tonoplast observed in intact vacuoles extracted from leaf tissue. Vacuoles from non-transformed WT plants are shown as negative control. Images of transmitted light (left), GFP fluorescence (centre) and merge of both (right). Images are representative of three biological replicates. Box plot represents Pearson's correlation coefficient. For **(a)** control $n = 4$ roots; quantification $n = 36$ vesicles from root meristem cells from 4 plants; for **(b)** BFA treated $n = 10$ roots; quantification, $n = 19$ cells from 4 plants. Box plots show centrelines medians; box limits indicate the 25th and 75th percentiles; whiskers extend to the minimum and maximum. For **(c)** BFA treated $n = 6$ roots; **(d)** BFA treated $n = 5$. Images are representative confocal images of 7 day old seedlings grown on $\frac{1}{2}$ MS plates in growth condition 1. Scale bars, 20 μm ((**a-d**) overview), 10 μm (**a-d** (inset)).

Reporting Summary

Nature Portfolio wishes to improve the reproducibility of the work that we publish. This form provides structure for consistency and transparency in reporting. For further information on Nature Portfolio policies, see our [Editorial Policies](#) and the [Editorial Policy Checklist](#).

Statistics

For all statistical analyses, confirm that the following items are present in the figure legend, table legend, main text, or Methods section.

n/a Confirmed

- The exact sample size (n) for each experimental group/condition, given as a discrete number and unit of measurement
- A statement on whether measurements were taken from distinct samples or whether the same sample was measured repeatedly
- The statistical test(s) used AND whether they are one- or two-sided
Only common tests should be described solely by name; describe more complex techniques in the Methods section.
- A description of all covariates tested
- A description of any assumptions or corrections, such as tests of normality and adjustment for multiple comparisons
- A full description of the statistical parameters including central tendency (e.g. means) or other basic estimates (e.g. regression coefficient) AND variation (e.g. standard deviation) or associated estimates of uncertainty (e.g. confidence intervals)
- For null hypothesis testing, the test statistic (e.g. F , t , r) with confidence intervals, effect sizes, degrees of freedom and P value noted
Give P values as exact values whenever suitable.
- For Bayesian analysis, information on the choice of priors and Markov chain Monte Carlo settings
- For hierarchical and complex designs, identification of the appropriate level for tests and full reporting of outcomes
- Estimates of effect sizes (e.g. Cohen's d , Pearson's r), indicating how they were calculated

Our web collection on [statistics for biologists](#) contains articles on many of the points above.

Software and code

Policy information about [availability of computer code](#)

Data collection

CryoNanoSIMS instrument at the Laboratory for Biological Geochemistry at EPFL, Switzerland were used to acquire CryoNanoSIMS images. Confocal images were taken using Leica Stellaris 5 WLL inverted confocal microscope and the LAS X (2022) software. Spinning disc movies were generated using CSU-W1 Yokogawa spinning disk head fitted to a Nikon Eclipse Ti-E-inverted microscope.

Data analysis

CryoNanoSIMS analyses were performed using L'IMAGE© software version 10-15-2021 (developed by Dr. Larry Nittler). Confocal and spinning disk images were processed using ImageJ 1.54f (Rasband, W.S., ImageJ, U.S. NIH, Bethesda, Maryland, USA, <http://imagej.nih.gov/ij/>, 1997-2012) and in-built plugins of Fiji. Co-localization determined using Coloc2 plugin in Fiji. Statistical analyses were performed using OriginPro (Version 2023b, OriginLab Corporation, Northampton, MA, USA) and GraphPad software (Prism 10). The SEM images were processed with levels setting in Photoshop (Version 25.11.0). Figures were prepared using Adobe Illustrator (Version 28.7.1).

For manuscripts utilizing custom algorithms or software that are central to the research but not yet described in published literature, software must be made available to editors and reviewers. We strongly encourage code deposition in a community repository (e.g. GitHub). See the Nature Portfolio [guidelines for submitting code & software](#) for further information.

Data

Policy information about [availability of data](#)

All manuscripts must include a [data availability statement](#). This statement should provide the following information, where applicable:

- Accession codes, unique identifiers, or web links for publicly available datasets
- A description of any restrictions on data availability
- For clinical datasets or third party data, please ensure that the statement adheres to our [policy](#)

All associated pre-processed and processed data for the CryoNanoSIMS and fluorescence images are available in the latest version of <https://doi.org/10.5281/zenodo.1405406>. Full versions of all gels and blots presented are provided in Supplementary Figure 1. Source data are provided with this paper for all the main and extended data figures that contain analyses.

Research involving human participants, their data, or biological material

Policy information about studies with [human participants or human data](#). See also policy information about [sex, gender \(identity/presentation\), and sexual orientation](#) and [race, ethnicity and racism](#).

Reporting on sex and gender	NA
Reporting on race, ethnicity, or other socially relevant groupings	NA
Population characteristics	NA
Recruitment	NA
Ethics oversight	NA

Note that full information on the approval of the study protocol must also be provided in the manuscript.

Field-specific reporting

Please select the one below that is the best fit for your research. If you are not sure, read the appropriate sections before making your selection.

Life sciences Behavioural & social sciences Ecological, evolutionary & environmental sciences

For a reference copy of the document with all sections, see nature.com/documents/nr-reporting-summary-flat.pdf

Life sciences study design

All studies must disclose on these points even when the disclosure is negative.

Sample size	Sample size was determined based on the type of analysis. The CryoNanoSIMS experiments being low-throughput, a minimum of n=3 roots per condition per time point were chosen as minimum replicate numbers. A control and treatment sample for each of the conditions tested were tested in parallel in the same run. Growth and root phenotyping experiments had larger sample sizes per biological replicate as stated in their respective figure legends. Protein localization experiments were performed on minimum n=5 seedlings for each treatment and compared against internal controls (mock).
Data exclusions	Data were not excluded from analysis.
Replication	All replication experiments for CryoNanoSIMS were processed following the cryo-workflow described in the methods. The quantifications were performed pooling different runs and stringent parameters for selection of regions of interest have been described in detail in the methods section. For the different treatments, all conditions were replicated and compared against a control (mock) for protein localization patterns. All experiments were replicated and all attempts at replication were successful.
Randomization	Seedlings used for imaging were selected randomly, however all roots were analyzed equally with no sub-sampling and therefore, there was no requirement for randomization.
Blinding	Blinding was not possible as experimental conditions needed rigorous tracking throughout the CryoNanoSIMS workflow. Quantifications were performed applying the same approach equally to all conditions and replicates.

Reporting for specific materials, systems and methods

We require information from authors about some types of materials, experimental systems and methods used in many studies. Here, indicate whether each material, system or method listed is relevant to your study. If you are not sure if a list item applies to your research, read the appropriate section before selecting a response.

Materials & experimental systems

n/a	Involved in the study
<input type="checkbox"/>	<input checked="" type="checkbox"/> Antibodies
<input checked="" type="checkbox"/>	<input type="checkbox"/> Eukaryotic cell lines
<input checked="" type="checkbox"/>	<input type="checkbox"/> Palaeontology and archaeology
<input checked="" type="checkbox"/>	<input type="checkbox"/> Animals and other organisms
<input checked="" type="checkbox"/>	<input type="checkbox"/> Clinical data
<input checked="" type="checkbox"/>	<input type="checkbox"/> Dual use research of concern
<input type="checkbox"/>	<input checked="" type="checkbox"/> Plants

Methods

n/a	Involved in the study
<input checked="" type="checkbox"/>	<input type="checkbox"/> ChIP-seq
<input checked="" type="checkbox"/>	<input type="checkbox"/> Flow cytometry
<input checked="" type="checkbox"/>	<input type="checkbox"/> MRI-based neuroimaging

Antibodies

Antibodies used

Antibodies were prepared against the peptide “RSFRKEHRGMSWPE” of the C-terminal region of SOS1. Primary antibody (purified antiSOS1 antibodies, 1:2,000 dilution; antiEpsilon subunit of tonoplast H+ATPase antibody AS07 213 from Agrisera, 1:10,000 dilution). Secondary antibody: Horseradish peroxidase (HRP)-conjugated goat anti-mouse secondary antibody was used diluted 1:10,000 in TBS-T.

Validation

The SOS1 antibodies were validated by antiserum detection by Western blot using purified SOS1 isolated from yeast.

Plants

Seed stocks

Seeds of mutants and organelle markers were sourced from NASC - The European Arabidopsis Stock Centre.

Novel plant genotypes

Two independent constructs were generated for confirmation of protein localization. Complementation of function was performed by Agrobacterium mediated transformation of wild-type and mutant plants with the genomic constructs and analyses of independent lines.

Authentication

The mutant allele and marker lines for sub-cellular structures have been previously well characterized. Seeds for transgenic lines were verified by selection marker (seed coat fluorescence or antibiotics) and confirmed to be homozygous before analyses.